

Bayesian optimization for the informed placement of multi-array brain electrodes in advanced visual cortical prostheses

MSc Thesis

Odysseas Papakyriakou

odysseas.papakyriakou@gmail.com

May 2024

1st supervisor: Chris Klink

2nd supervisor: Daan van Rooij

Master of Science in Artificial Intelligence
Graduate School of Natural Sciences
Utrecht University, the Netherlands



**Utrecht
University**

Abstract

Recent advances in neurotechnology and artificial intelligence have paved the way for restoring a rudimentary form of vision in blind patients by electrically stimulating the visual areas of the brain. Finding the proper location in the brain in a non-surgical way poses a significant challenge for the planning and implementation of visual cortical prostheses. This research presents a Bayesian optimization pipeline for the informed placement of multi-array brain electrodes in advanced visual cortical prostheses. The procedure is based on individual MRI scans and retinotopy data from the Human Connectome Project, allowing to find the array parameters and the exact brain location that provide the closest match to a predetermined visual field coverage. The procedure is tested for multiple arrays of two types in the V1 area of the brain: 5 arrays of a theoretical three-dimensional type of 1000 electrodes in each array; and 16 two-dimensional arrays of 100 electrodes each, modelling the Utah array, which is widely used in research and clinical practice. The pipeline can easily be configured for an arbitrary number of arrays, to simulate different array designs, to cover a specific part of the visual field, and to include placement in different cortical visual areas. Results show that the inclusion of additional arrays substantially increases the visual field coverage compared to using one array, and that using individual anatomical scans offers a great advantage compared to average brain solutions. Therefore, the pipeline can be a valuable tool in designing and planning novel types of brain-interfacing visual cortical prostheses.

Keywords: Bayesian optimization, visual prostheses, brain computer interface, MRI, retinotopy

Contents

Abstract	2
1 Introduction	5
1.1 Motivation	5
1.2 Research objectives	6
2 Theoretical background	9
2.1 The human visual system	9
2.2 Visual cortical prostheses	11
2.3 Bayesian optimization	13
2.3.1 General information about optimization	14
2.3.2 Bayesian optimization	14
3 Methodology	20
3.1 Bayesian optimization for multi-array brain electrodes	20
3.2 Flow of the optimization pipeline	24
3.2.1 Dataset and extraction of relevant brain coordinates	25
3.2.2 Build and virtually implant grid based on insertion trajectory	25
3.2.3 Extract pRFs and create phosphene map	27
3.2.4 Compare predicted phosphene map with the target map and get cost	27
3.2.5 Evaluate the grid's validity	30
4 Experiments	31
4.1 Experiment 1: Multiple 3d arrays vs one, based on individual scans	32
4.1.1 Experimental set-up and analysis	32
4.1.2 Results	33
4.1.3 Discussion	35
4.2 Experiment 2: Multiple 3d arrays based on individual scans vs multiple 3d arrays based on the average brain scan	36
4.2.1 Experimental set-up and analysis	36
4.2.2 Results	36
4.2.3 Discussion	38
4.3 Experiment 3: Multiple Utah arrays vs multiple 3d arrays, based on individual scans	39
4.3.1 Experimental set-up and analysis	39
4.3.2 Results	40
4.3.3 Discussion	45
5 General discussion	47
5.1 Relation to theory and previous research	47
5.2 Societal relevance and clinical implications	48
5.3 Limitations and future research	48
6 Conclusion	49

References	50
A Experiment 1 results	54
A.1 Descriptive results	54
A.2 Assumptions for repeated measures ANOVA	54
A.3 Post-hoc pairwise comparisons with Tukey's HSD test	56
B Experiment 2 results	56
B.1 Descriptive results	56
B.2 Assumptions for paired samples t-test	56
C Experiment 3 results	57
C.1 Descriptive results	57
C.2 Assumptions for paired samples t-test	57

1 Introduction

1.1 Motivation

Vision plays an important role in people’s experience of the world, so blindness can have a substantial impact on many people’s lives. Additionally, the amount of people around the world that is affected by visual impairments is rising. Globally, it is estimated that around 43 million people live with complete blindness (Orbis international, 2021), while in the Netherlands this number is estimated to be around 77.000 (Limburg & Keunen, 2009). The tools attempting to facilitate the daily lives of blind and visually impaired people vary, including a specifically designed reading and writing system called Braille, the use of guidance animals, probing canes and specifically designed paths on the streets, as well as computer assistive technologies, like screen readers (Curing retinal blindness foundation, 2023). However, although these tools may be of profound assistance, they do not restore or improve people’s vision.

The present research is part of a broad research effort for restoring a rudimentary form of vision in patients with acquired blindness. Particularly, it is embedded within the INTENSE research project (INTENSE: Innovative Neurotechnology for Society, 2023), devoted to developing brain implants to improve the lives of people who are blind, deaf, paralyzed, or have epilepsy. Brain Computer Interfaces (BCIs) for blind people aim at generating a visual percept, or phosphenes, directly in the brain by electrically stimulating the neural tissue, thus enabling them to experience a rudimentary visual form of the environment. Phosphenes refer to small dots of light that are being perceived by the individual when using such a BCI, and they aim to reflect the most relevant features of a scene so that useful visual information is communicated (van der Grinten et al., 2024).

Visual cortical prostheses are based on the retinotopic organization of the visual system. Retinotopic organization means that the visual field is represented into the visual part of the brain in a systematic manner, such that there is a consistent correspondence between the location of the neurons in the visual cortex and the location of the visual space they represent (Gazzaniga, Ivry, & Mangun, 2019). This allows a visual BCI to generate a phosphene percept at a given location of the visual field by stimulating the corresponding electrodes that are surgically placed in the visual cortex (van Hoof, 2022). As such, the number and distribution of the electrodes plays a critical role into how representative of the visual field the resulting artificial vision will be. Even though previous simulation research has found that an increasing number of electrodes is not always optimal for mobility performance (de Ruyter van Steveninck et al., 2022), having the possibility to optimally place a large number of electrodes across different arrays could be highly beneficial depending on the goal of the application. (Chen et al., 2023).

The electrode implantation procedure for a visual cortical prosthesis poses some major challenges. One of the most important decisions when implanting a visual prosthesis is the location where the device will interact with the brain, since this determines the generated artificial vision. Knowing the retinotopic organization of the brain allows to predict the visual field coverage of artificial vision when the electrodes are placed at a certain location. Research by (Benson et al., 2012; Benson, Butt, Brainard, & Aguirre, 2014), has provided a procedure based on MRI data to model the functional organization of the retinotopic cortex, in areas V1, V2, and V3. Importantly, the retinotopic organization remains present in patients that became blind later in life, but it may be greatly reduced in congenitally blind patients. After having identified the retinotopic organization

in visual cortex using the procedure by (Benson et al., 2014), another crucial challenge is to optimally place the electrode arrays in a way to generate the desired artificial vision. Having merely identified the retinotopic cortical organization is not enough, since small differences in the angle or location of the electrodes within this area can result in great differences in the generated phosphenes. Additionally, since the electrode implantation procedure requires surgery, the electrodes cannot be easily moved after the initial placement. This accentuates the need to carefully plan and optimize the implantation location non-invasively, so that artificial vision is as functional as possible. This research contributes to this challenge by implementing a Bayesian optimization procedure for the placement of the array electrodes.

The most widely used type of such electrode arrays implemented in human trials is the Utah array (Zardini, Rostami, Najafi, Hetrick, & Ahmed, 2021), but long-term studies in animals have shown that the number of phosphene-generating electrodes decreases substantially over time (Chen et al., 2023). Other types of arrays, like linear depth probes, or three-dimensional arrays are also being investigated, primarily in animal studies, aiming to increase the functioning electrode count and to overcome the long-term negative effects of using a large number of Utah arrays.

Research by Fernández et al. (2021) applied the aforementioned procedure by Benson et al. (2014) in a clinical setting where they implanted an array of 96 electrodes into the cortical visual area of a blind patient, while mapping the location of the generated phosphenes using an experimental stimulus protocol. Although this procedure was effective in mapping the phosphene locations evoked by the electrodes after implantation, it cannot optimize the array location before implantation based on predicted phosphene locations.

Previous research by van Hoof et al. (2024), has implemented a Bayesian optimization procedure aiming to find the best location of a (yet) non-existing three-dimensional array, with shape 10x10x10 in different visual centers of the brain, using individual anatomical scans. The procedure takes into account the predicted phosphene map, thus placing the array at the optimal location, while also determining the best parameters for some aspects of the design of the array. However, the part of the visual field that can be covered by stimulating electrodes only with one array is limited and is mostly in the central part of the visual field. Implanting an increasing number of arrays allows for a more detailed representation of the visual field that can also include its more peripheral parts (Chen et al., 2023). Additionally, the array configuration in this implementation does not align with the electrode arrays that are widely used in research or clinical settings, like the ones produced by large array manufacturers, for example Blackrock-Neurotech (2024), or Neuronexus (2024). As such, the practical impact of this implementation is limited.

1.2 Research objectives

The main objective of this research is to re-design and expand the Bayesian optimization algorithm proposed by (van Hoof et al., 2024), to make it suitable for the planning of different electrode types and for the placement of multiple brain electrode arrays. The procedure is guided by the difference between a target, or desired, visual field coverage and the predicted phosphenes generated by the simulated array placement in the V1 area, which is the brain’s first cortical center for vision. It maximizes the patient’s visual field coverage by minimizing the difference between the predicted phosphenes and

the target coverage, and it can easily be adapted to cover different parts of the visual field, as well as to include other visual areas, like V2 or V3. Specifically, the procedure considers individual anatomical scans to account for differences in the organization of visual brain centers, while also implementing different types of array designs. This leads to the formulation of the following main research question:

Main research question: How can a Bayesian optimization algorithm facilitate the efficient placement of multiple electrode arrays of different designs, in the V1 brain area, for a BCI designed to generate artificial vision?

To explore the main research question holistically, while keeping in mind the goal of making the results of this research as transferable as possible to future clinical applications, the main research question is broken down into 3 sub-questions.

Sub-question 1: Given the individual anatomical scans, what is the added benefit of using multiple arrays of shape 10x10x10 instead of the 1 that was previously used (van Hoof et al., 2024), and what is the contribution of each array after placement in the V1 brain area?

Expected result: Given that a larger number of arrays has the potential to generate a larger number of phosphenes across the visual field, it is expected that the visual field coverage will increase as the number of arrays increases. Additionally, the optimization procedure is able to estimate the added benefit of each individual array as well as to find the optimal array parameters. Therefore, the procedure is also expected to find the best number of arrays and their parameters for meeting the requirements of a given application.

To answer sub-question 1, the effect of varying the number of optimally placed arrays on the metrics of the generated phosphenes will be estimated with statistical comparisons.

The second sub-question aims to explore the benefit of optimizing the array placement based on each individual’s anatomical scan. Given that this process is costly in computation and time, one could argue that since the visual brain areas are in a similar location across individuals, one could implement the optimization procedure on the average brain, and then implant the optimal configuration for the average brain in all individuals.

Sub-question 2: Given the optimal placement for multiple arrays of shape 10x10x10 in the V1 brain area based on the average brain, what is the added benefit of an individualized approach based on individual anatomical scans?

Expected result: Since there is some anatomical difference across individuals, it is expected that the generated phosphenes from the individualized approach will provide a better coverage of the visual field compared to the average ap-

proach. The optimization procedure allows to quantify exactly how much this added benefit of the individualized approach is in terms of the visual field coverage.

Lastly, aiming to inform potential clinical applications, the third sub-question relates to implementing the optimization procedure with an array configuration that is widely used in practice nowadays. As mentioned previously, the implementation by van Hoof et al. (2024) has used a hypothetical design for an array of 1000 electrodes with a shape of $10 \times 10 \times 10$. However, such large number of three-dimensional electrode probes are not yet realistic for stimulating electrodes, although there have been some similar designs for recording electrodes (Rios, Lubenov, Chi, Roukes, & Siapas, 2016). The most widely used electrode array for neural stimulation is the Utah array (Zardini et al., 2021), which has a two-dimensional shape of $1 \times 10 \times 10$. Sub-question three explores the differences between implementing the procedure with a more realistic two-dimensional array of shape $1 \times 10 \times 10$, and with the aforementioned hypothetical three-dimensional array. Additionally, the ease with which the array parameters can be adjusted through the configuration file allows to model and compare the performance of new array designs that do not yet necessarily exists.

Sub-question 3: Given the the optimal placement for 16 Utah arrays of shape $1 \times 10 \times 10$ based on individual anatomical scans, what is the added benefit in the phosphene metrics of using the hypothetical three-dimensional arrays of shape $10 \times 10 \times 10$? The differences between these two array types is in the depth dimension, as well as the number of electrodes.

Expected result: Since a larger number of correctly placed electrodes results in a larger number of generated phosphenes, it is expected that the generated phosphenes resulting from the hypothetical three-dimensional array configuration will provide a better coverage of the visual field compared to the two-dimensional array that is widely used in research and clinical practice.

When exploring the hypothetical three-dimensional array in all these sub-questions, some of the array parameters are allowed to vary. All information about the array parameters, the development of the code, and the flow of the optimization are described in detail in section 3. The code is open source and can be found on this [GitHub link](#).

2 Theoretical background

2.1 The human visual system

To better understand the scope of this research, it is essential to have a fundamental understanding of how the human visual system works. An explanatory illustration is shown in figure 1, where the stimuli from each visual field end up at the contralateral sites of the brain. As becomes apparent, when light is projected onto the retina, optical information is converted to neural spiking activity by the photoreceptors of the eyes, the rods and the cones, and then transmitted via retinal ganglion cells to the lateral geniculate nucleus of the thalamus. From there, the information is conveyed to the primary visual cortex in the occipital lobe via thalamic synapses and then transferred to higher cortical areas in the brain. Blindness may occur from damage to any part of this path, so visual prostheses that aim to simulate vision electrically stimulate one of these parts depending on the underlying pathophysiology, but usually it involves the retina, the optic nerve, the nuclei of the thalamus dedicated to vision, or the visual cortex (van Hoof, 2022). This research is aimed for a cortical prosthesis that places electrodes on the primary visual cortex, in particularly area V1, to stimulate the necessary neurons in order to generate a given percept. Patients that are not congenitally blind are expected to have more developed visual centers than congenitally blind patients, therefore, such a cortical prosthesis would probably yield better results in people that have had experience seeing (Heitmann et al., 2023).

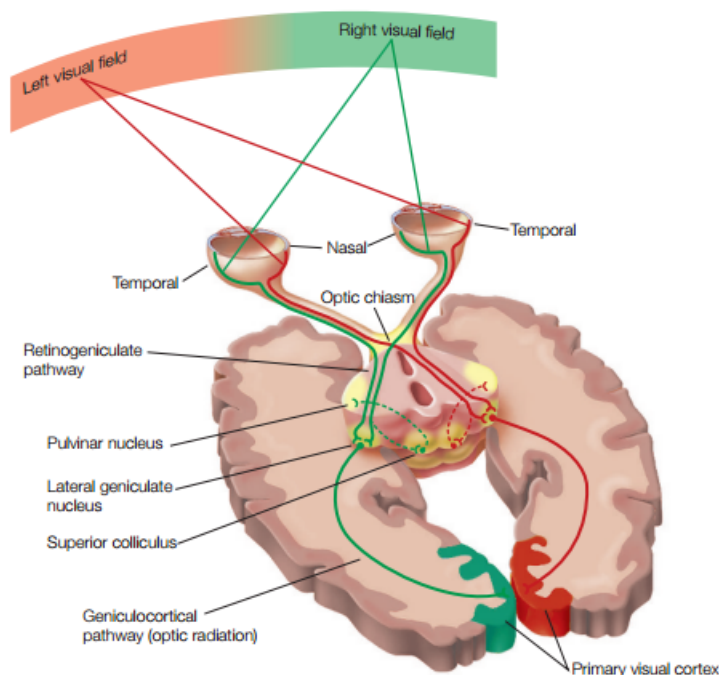


Figure 1. The human visual pathway. Image from Gazzaniga et al. (2019, p. 192).

Importantly, the visual system follows a retinotopic organization, meaning that the visual information captured from the retina of the eye is processed and represented in a way that maps the spatial layout of the visual field in a systematic manner. (Gazzaniga et al., 2019). Specifically, each point in the eye’s retina that captures visual information from the external world corresponds to a specific part of the visual field. This is possible

because neurons in the visual system only respond when a stimulus is presented in a specific region of space, called the receptive field of the neuron (Gazzaniga et al., 2019). Eccentricity refers to the distance of the stimulus from the fixation point (Kandel et al., 2014), where higher distance reflects higher eccentricity. At any given eccentricity, the visual stimulus can appear anywhere around 360° of visual angle, so this is referred to as the polar angle of the stimulus (Himmelberg, Winawer, & Carrasco, 2023). Figure 2a shows a retinal map as an example.

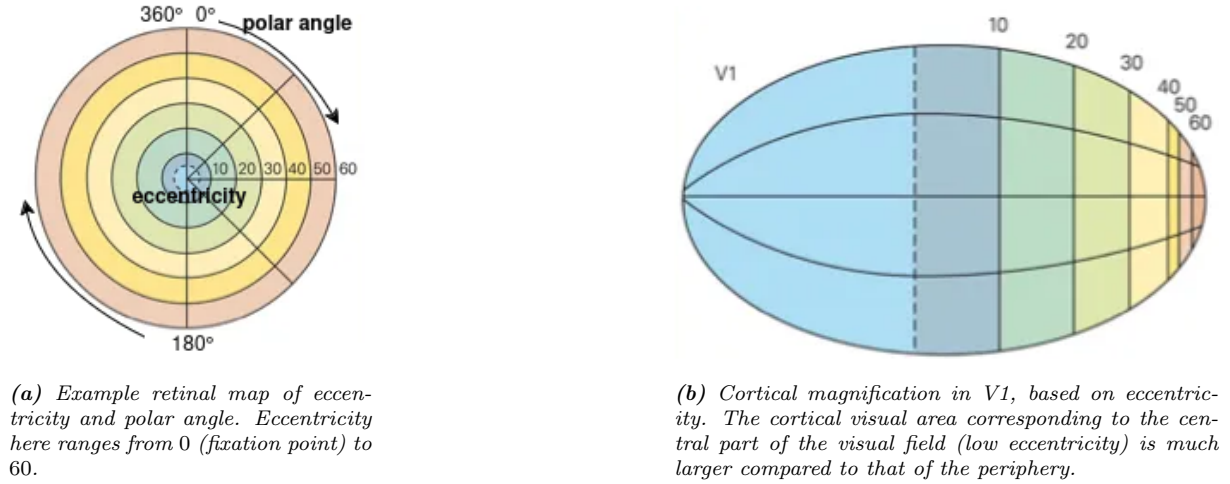


Figure 2. Illustration of retinal eccentricity (2a), and its relation to cortical magnification in the V1 brain area (2b). Images from Kandel et al. (2014, p. 567).

Another feature of topographic organization is cortical magnification, allowing humans to have a more focused and detailed perception of the central part of the visual field compared to the peripheral (Kandel et al., 2014). Neurally, this is reflected in a larger number of neurons with a receptive field that corresponds to the central part of the visual field compared to the peripheral part, which is also described as having a higher *density* of neurons devoted to processing information around the fixation point. An example illustration is shown in figure 2b. Additionally, the size of the receptive field changes along the visual system, becoming increasingly larger. Starting with the receptive field of the photoreceptors that seem to respond selectively to tiny dots in a very specific part of the visual space, the receptive fields in higher order cortical areas, like the temporal lobe, may encompass the entire hemifield (Kandel et al., 2014). The V1 brain area is a good candidate for the placement of a visual cortical prosthesis because its neurons have a smaller receptive field size compared to higher visual areas (Benson, Kupers, Barbot, Carrasco, & Winawer, 2021), which could allow for denser and more detailed representations of the visual field. At the same time, neurons' receptive field in V1 is not as small as that in the retina or the thalamus, thus offering a good balance between fine detail and visual field coverage.

The specificity with which neurons respond to the stimuli in the visual field provides a mapping between the brain area that is being electrically stimulated and the mental visual field to which the generated stimulus will appear. This allows visual cortical prostheses to generate a visual percept of the environment at a predicted location in the visual field. Importantly, electrically stimulating a neuron with a given receptive field, results in a phosphene percept at the corresponding visual field location regardless of whether there is a stimulus there. Therefore, for a BCI to help blind individuals restore some funda-

mental visual form of the environment, the location of the electrodes plays a determining factor, since it dictates the location of the visual field where the phosphene patterns are generated. Such a “phosphene map” describes the density and location in which individual phosphenes can be evoked in the visual field, while the exact characteristics of a single phosphene depend on the stimulation parameters, the design of the electrode, and the underlying brain tissue (van Hoof, 2022). As explained above in section 2.1, the visual cortex of each hemisphere receives information from the contralateral visual field. For cortical prostheses, this means that stimulating neurons in one hemisphere will elicit phosphenes in the contralateral visual field.

2.2 Visual cortical prostheses

Although the first reported case of eliciting a flickering visual perception by electrical cortical stimulation was in wounded soldiers as early as in 1918 (Niketeghad & Pouratian, 2018), the first systematic research to develop a visual cortical prosthesis was in 1968 (Brindley & Lewin, 1968). The technology at the time did not allow for generating percepts that match the visual scene, but the extracranial array of radio receivers allowed for the selective activation of intracranial electrodes, thus resulting in the perception of phosphenes in different areas of the visual field (Brindley & Lewin, 1968). Since then, a lot of developments have taken place, with the current desired state of a cortical visual prosthesis being illustrated in figure 3. To elicit a dynamic perception of the visual scene, a camera on the head captures a video which is processed by a mobile device and converted into interpretable signals. The electrode arrays then wirelessly receive these signals to stimulate the neural tissue accordingly (van Hoof, 2022).

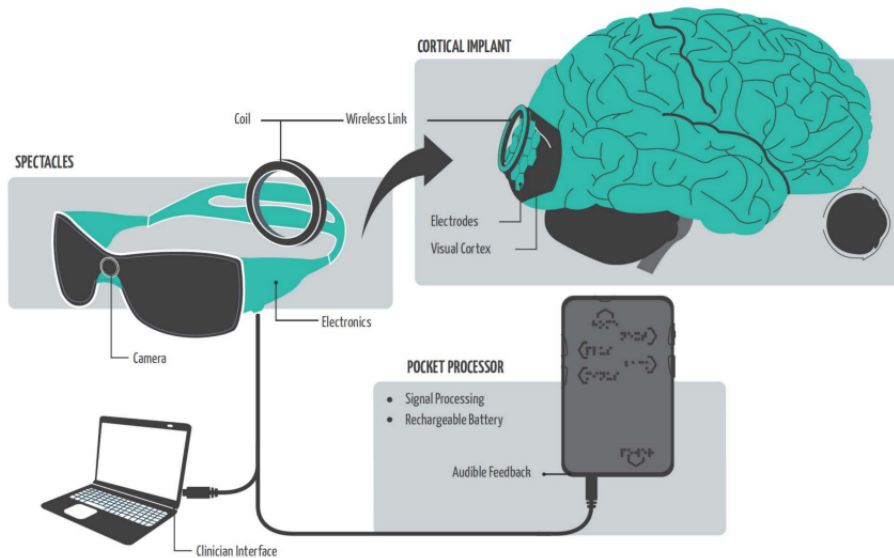


Figure 3. Overview of an ideal wearable cortical visual prosthesis. Image from van Hoof (2022, p. 25).

Recent research on visual restoration with cortical prostheses has made substantial progress in eliciting recognizable phosphene patterns. Starting from animal trials, Chen, Wang, Fernandez, and Roelfsema (2020) placed 1024 electrodes using 16 Utah arrays in areas V1 and V4 of the visual cortex in monkeys to induce the perception of shapes, motions, or letters. Results showed that monkeys were able to correctly identify the shown shapes, while saccade tracking of the monkeys’ eyes showed that the stimuli were presented at the intended location. The monkey retinotopy has been studied in depth

by Tootell, Switkes, Silverman, and Hamilton (1988), so the researchers could accurately stimulate the desired receptive fields, namely, the foveal and parafoveal regions of the lower right visual field. However, there is still some variability between the brain anatomy of different monkeys, and even more variability for humans in some visual areas (Benson et al., 2022), so trials with humans would ideally need to take the individual anatomy into consideration, especially if the goal is to elicit dynamic phosphene patterns coming from a changing environment through a video feed.

Human trials on visual restoration via a cortical prosthesis have mostly focused on surface brain electrodes (Dobelle, Mladejovsky, & Girvin, 1974; Beauchamp et al., 2020), so without penetrating into the cortex. Even though this resulted in the perception of one simple shape at a given time, when multiple electrodes were stimulated at the same time the phosphenes usually merged into larger ones, thus hindering shape recognition (Roelfsema, 2020). Probably, this is related to the fact that surface electrodes interact with large volumes of cortex, evoking a low spatial resolution of the perceived phosphene (Roelfsema, 2020). Additionally, the increased current strength that is necessary for phosphene perception from surface electrodes may be detrimental to the cortex (Roelfsema, 2020), while it is also strenuous to convey information about several objects or about a moving scene, thus rendering cortical stimulation with surface electrodes a suboptimal method.

To circumvent these shortcomings, Fernández et al. (2021) implanted an intracortical array of 96 penetrating microelectrodes in the visual cortex of a 57-year-old woman with complete blindness. The mean stimulation threshold for single electrodes was at $66.8 \pm 36.5 \mu A$, much less than the strength used in studies with surface electrodes. This played a significant role in the safety of the stimulation, as the subject did not have any complications after explantation at the end of the 6-month trial. Additionally, the subject was able to accurately perceive complex visual percepts generated not only by 2 electrodes, but also by different combinations of 3 to 16 electrodes distributed over the array. Impressively, the subject reported that the simultaneous stimulation of multiple electrodes elicited phosphene patterns that were easier to identify than the ones evoked by the stimulation of single electrodes. Lastly, a remarkable innovation of this research was the use of a visual encoder to dynamically stimulate different combinations of electrodes based on the visual scene, as this is captured by a head-mounted camera and spatial and temporal image processors.

One consideration regarding the aforementioned research is that the one implanted array with its 96 electrodes had a very limited coverage of less than 4 visual degrees eccentricity of the lower left part of the visual field, as is shown in figure 4, taken from the authors' paper (Fernández et al., 2021). Ideally, in a situation where the phosphenes represent the visual scene, the perceived phosphene locations would match the location of the objects in the visual field in a larger eccentricity range, not only the very central part. This accentuates the need to incorporate more electrode arrays to cover a wider part of the visual field.

Research by van Hoof et al. (2024) explored the latter issue by trying to optimize the planning of the electrode placement on the visual cortex. The aforementioned research by Fernández et al. (2021) merely used the procedure by Benson et al. (2012) to generate a probabilistic retinotopic map of the brain based on the patient's anatomical scans. Although this procedure gives functional information in volumetric space, allowing to infer what part of the visual cortex corresponds to which point in space, it does not plan in advance the exact placement location of the electrodes and the generation of phosphenes.

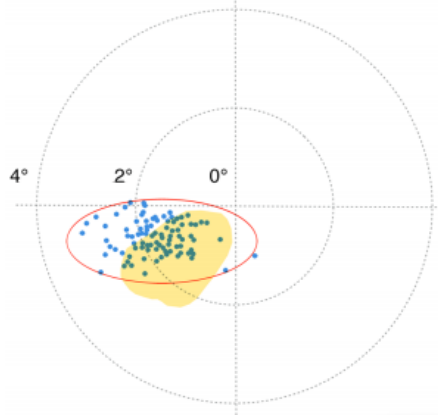


Figure 4. Location of perceived phosphenes (blue dots) and expected location of the phosphenes (yellow). Image from Fernández et al. (2021, p. 7).

After acquiring a retinotopic map using Benson et al.’s (2012) procedure, van Hoof et al.’s (2024) research, used Bayesian optimization to get the location and angle of the electrodes that yield predictive phosphene sizes and locations as close to the desired ones. In addition to the location of the electrodes, this implementation also optimizes the design of the electrode array, by allowing to vary two parameters: the length of the electrode shank on which the electrodes are located, and by extension the distance between the electrodes on the shank (larger shank length means larger distance between electrodes on the shank); the distance between the first contact point of the electrode shank and the point where the shank penetrates the cortex. This process succeeds in automatically finding the electrode configuration and implantation trajectory that optimally matches a preset ideal phosphene distribution within some predetermined practical constraints, for example that there cannot be electrodes outside of grey matter area (van Hoof et al., 2024).

This optimization procedure has been implemented with a hypothetical design of a three-dimensional array with 1000 electrodes using a configuration of 10x10x10, modelling 10 combs of 10 electrode shanks, each of 10 contacts points. It was tested on 362 human hemispheres, so 181 subjects, using anatomical and retinotopy data from the Human Connectome Project 7 Tesla retinotopy dataset (van Hoof, 2022). Even though the number of electrodes is significantly larger than the 96 that were used by Fernández et al. (2021), the use of only one array still limits the amount of visual field that can be covered. Additionally, there is no known array design with this configuration that is used in research or clinical settings.

2.3 Bayesian optimization

Section 2.3 describes the technical details about Bayesian optimization. Sub-section 2.3.1 starts with some general information about optimization theory, motivating the choice for the Bayesian optimization framework in sub-section 2.3.2. These sections provide a comprehensive description of the theory and the mathematics of Bayesian optimization, so the readers could skip to the methodology section, 3, to read about the implementation of the optimization procedure for this research.

2.3.1 General information about optimization

In optimization problems, the goal is to find the set of input parameters that optimize a specific objective function, often denoted as $f(x)$ where x represents the parameters or variables being optimized. Formally,

$$\begin{aligned} & \underset{\mathbf{x} \in A}{\text{optimize}} && f(x) \\ & \text{subject to} && g_i(x) \leq 0, \quad i = 1, \dots, m \\ & && h_j(x) = 0, \quad j = 1, \dots, p \end{aligned} \tag{1}$$

where:

$f : A \rightarrow \mathbb{R}$ = the objective function to be optimized for some set A , where usually $A \subset \mathbb{R}^n$ over the n -variable vector \mathbf{x}
 $g_i(x) \leq 0$ = the inequality constraints
 $h_j(x) = 0$ = the equality constraints
 $m \geq 0$ and $p \geq 0$

The desired parameters \mathbf{x}_0 optimize the function f such that either $f(\mathbf{x}_0) \leq f(\mathbf{x}) \forall \mathbf{x} \in \mathbb{R}$, or $f(\mathbf{x}_0) \geq f(\mathbf{x}) \forall \mathbf{x} \in \mathbb{R}$, where the former case is a minimization problem and the latter a maximization.

When the objective function f is known, and some assumptions are met, the optimization problem can be approached by applying deterministic methods. For deterministic optimization, it is often assumed that A is compact, and that f is Lipschitz-continuous and differentiable over the search space, such that $\forall x, z \in A, |f(x) - f(z)| \leq l \cdot \|x - z\|$ for some constant $l \geq 0$. The compactness assumption states that the solution set A is both closed and bounded, and together with the continuity assumption they guarantee that a solution exists, so that $\exists x^* \in A$ such that $f(x^*) = \sup_{x \in A} f(x)$ (Lizotte, 2008). A distinction is drawn between global optimization, referring to the absolute optimum in A , and local optimization, referring to a local optimum in the neighborhood of a given initial point \mathbf{x}_0 . Deterministic optimization methods follow a systematic approach, often relying on the known properties of the objective function f , like its gradients, while they assume that it is precisely known at each evaluated point, so they do not incorporate uncertainty.

2.3.2 Bayesian optimization

When there is no analytical expression for f , as is the case with the optimization problem of this research, and thus its derivatives are unknown, $f(x)$ is called a black box function. This means that it cannot be optimized with deterministic, first- and second-order methods like gradient descent or Newton's method (Frazier, 2018). As such, black box functions are necessarily optimized with iterative, derivative-free algorithms that can be applied when f lacks a known special structure like concavity or linearity. Bayesian optimization is such an optimization method that is particularly useful when the objective function f is computationally expensive to evaluate (Frazier, 2018).

Since there is no analytical expression for the objective function, Bayesian optimization maintains a probabilistic model about f , also called a *surrogate model*, and designs what is called an *acquisition function* to determine at which point in the search space to evaluate the function next. The surrogate model should be able to be sampled efficiently, to encode prior beliefs about the objective function, to update those beliefs according to

the laws of probability as new data about the function accumulates, and to guide the progress of the optimization procedure (Lizotte, 2008).

As the name implies, Bayesian optimization is based on Bayes' theorem, stating that the posterior probability of a model (or theory, or hypothesis) M given some data (or observations, or evidence) D equals the likelihood of D given M , multiplied by the prior probability of M and divided by the marginal likelihood of D , as shown in equation 2. The marginal likelihood is a likelihood function, ie. the joint probability of observed data as a function of the parameters of a statistical model, integrated over the parameter space, and it represents the probability of generating the observed sample from a prior. In essence, this marginal likelihood is a normalization parameter and it helps to calculate a specific condition probability. However, the goal is to optimize a quantity, ie. the objective function, so this normalization term can be dropped, thus making the posterior proportional to the likelihood times the prior (Brochu, Cora, & Freitas, 2010).

$$P(M|D) = \frac{P(D|M)P(M)}{P(D)}, \text{ Posterior} = \frac{\text{Likelihood} \times \text{Prior}}{\text{Marginal likelihood}} \quad (2a)$$

$$P(M|D) \propto P(D|M)P(M), \text{ Posterior} \propto \text{Likelihood} \times \text{Prior} \quad (2b)$$

Applying the general form of Bayes' theorem shown in equation 2 to Bayesian optimization, the prior represents our belief about the objective function, which takes a sample for each parameter from the search space and returns a cost. Defining \mathbf{x}_i as the i th sample vector and $f(\mathbf{x}_i)$ as the cost of the objective function at \mathbf{x}_i , the algorithm accumulates observations $\mathcal{D}_{1:t} = \{\mathbf{x}_{1:t}, f(\mathbf{x}_{1:t})\}$, and the prior distribution $P(f)$ is combined with the likelihood function $P(\mathcal{D}_{1:t}|f)$, to produce the posterior distribution, as shown in equation 3 (Brochu et al., 2010). Conceptually, this captures the likelihood of the objective function given the sample observations and our prior beliefs about the objective function.

$$P(f|\mathcal{D}_{1:t}) \propto P(\mathcal{D}_{1:t}|f)P(f) \quad (3)$$

As becomes apparent, modelling the prior of the objective function, or the surrogate model, plays a crucial role in the optimization procedure. Particularly, it provides a probabilistic estimate of where the true objective function may have better values, thus allowing the optimization algorithm to efficiently explore the search space. Additionally, the surrogate model also quantifies the uncertainty of unobserved areas, allowing to direct the search towards regions that have not been explored. GP priors have shown to perform very well in Bayesian optimization, since they are continuous, homogeneous, and they describe the likely values of f and their uncertainty with the mean and variance (Brochu et al., 2010).

A Gaussian process is an extension of the multivariate Gaussian distribution to an infinite-dimension stochastic process for which any finite combination of dimensions will be a Gaussian distribution, thus defining a distribution over functions (Frazier, 2018). Therefore, each draw from a GP is a multivariate Gaussian function, where in the context of Bayesian optimization it attempts to model the objective function, thus returning the mean and variance of a multivariate Gaussian distribution over the possible values of f at the sample vector \mathbf{x} . GPs are completely specified by their mean $m(\mathbf{x})$ and covariance $k(\mathbf{x}, \mathbf{x}')$ functions of a real process $f(\mathbf{x})$, as shown in equation 4.

$$\begin{aligned} m(\mathbf{x}) &= \mathbb{E}[f(\mathbf{x})] \\ k(\mathbf{x}, \mathbf{x}') &= \mathbb{E}[(f(\mathbf{x}) - m(\mathbf{x}))(f(\mathbf{x}') - m(\mathbf{x}'))] \end{aligned} \quad (4)$$

This allows to define the GP with the formula in 5.

$$f(\mathbf{x}) \sim \mathcal{GP}(m(\mathbf{x}), k(\mathbf{x}, \mathbf{x}')) \quad (5)$$

The mean function for the prior can be arbitrarily chosen, but conventionally it is set to 0, while the covariance function must be a positive definite function to ensure the existence of all finite-dimensional distributions (Rasmussen & Williams, 2005). Therefore, the positive definiteness of $k(\mathbf{x}, \mathbf{x}')$ ensures the positive (semi-)definiteness of all covariance matrices Σ (Rasmussen & Williams, 2005), appearing in the exponent of the probability density function of the multivariate Gaussian distribution with k dimensions shown in formula 6, where the mean vector $\boldsymbol{\mu}$ and the covariance matrix Σ are the free parameters. One of the attractive properties of GPs is that they fulfill the *marginalization property*, such that if the GP specifies $(y_1, y_2) \sim \mathcal{N}(\boldsymbol{\mu}, \Sigma)$, then it must also specify $(y_1) \sim \mathcal{N}(\mu_1, \Sigma_{11})$. This means that the addition of novel points does not influence the distribution of existing points, allowing to focus on the distribution of only observed data points with the rest of unobserved points being marginalized out, achieving a finite amount of computation for inference (Quadrianto, Kersting, & Xu, 2010).

$$P(\mathbf{x}|\boldsymbol{\mu}, \Sigma) \sim \mathcal{N}(\boldsymbol{\mu}, \Sigma) = \frac{1}{\sqrt{(2\pi)^k |\Sigma|}} \exp\left(-\frac{1}{2}(\mathbf{x} - \boldsymbol{\mu})^T \Sigma^{-1}(\mathbf{x} - \boldsymbol{\mu})\right) \quad (6)$$

where:

$$\begin{aligned} \boldsymbol{\mu} &\in \mathbb{R}^k \\ \Sigma &\in \mathbb{R}^{k \times k} \end{aligned}$$

$|\Sigma| \equiv \det(\Sigma)$ is the determinant of Σ , also known as the generalized variance

The covariance function $k(\cdot, \cdot)$ bears an essential role in GPs because its continuity properties determine the continuity properties of the functions sampled from the GP (Quadrianto et al., 2010). Importantly, it specifies the covariance $cov(\cdot, \cdot)$ between pairs of random variables, as shown in equation 7. Because the estimations of the function values $f(x_i)$ are often noisy, this can be incorporated into the covariance matrix by adding Gaussian noise $\epsilon_i \sim \mathcal{N}(0, \sigma_n^2)$ to the covariance of two random samples, thus $y_i = f(\mathbf{x}_i) + \epsilon_i$. The Gaussian noise matrix $\sigma_n^2 I$ has the variance σ_n^2 in the diagonal and zeros elsewhere, indicating the additive independent and identically distributed assumptions between the noise of different samples (Quadrianto et al., 2010). The noise can be directly added to the model since the sum of Gaussian variables is also a Gaussian (Rasmussen & Williams, 2005).

$$cov(f(\mathbf{x}_p), f(\mathbf{x}_q)) = k(\mathbf{x}_p, \mathbf{x}_q) + \sigma_n^2 I \quad (7)$$

where:

- \mathbf{x}_p and \mathbf{x}_q represent two different sample vectors.
- $f(\mathbf{x})$ is the observed function given the sampled vector \mathbf{x} .
- σ_n^2 is the variance of the random variables.
- I is the identity matrix, with 1s on the diagonal and zeros elsewhere.

The covariance matrix \mathbf{K} then is defined as shown in equation 8, which also incorporates the noise in the function values $f(\mathbf{x})$. In a noise-free environment, where the function values can be estimated exactly, the diagonal values of this matrix would be 1, since each point would be perfectly correlated with itself.

$$\mathbf{K} = \begin{bmatrix} k(\mathbf{x}_1, \mathbf{x}_1) & \cdots & k(\mathbf{x}_1, \mathbf{x}_t) \\ \vdots & \ddots & \vdots \\ k(\mathbf{x}_t, \mathbf{x}_1) & \cdots & k(\mathbf{x}_t, \mathbf{x}_t) \end{bmatrix} + \sigma_n^2 I \quad (8)$$

One of the most widely used covariance functions is the Radial Basis Function (RBF), also known as the Squared Exponential, shown in formula 9. This RBF kernel ensures the smoothness of the covariance matrix by generating large output values for x_p , x_q inputs that are closer to each other and smaller values for inputs that are further away (Quadrianto et al., 2010).

$$k(\mathbf{x}_p, \mathbf{x}_q) = \sigma_f^2 \exp \left(-\frac{1}{2\ell^2} \|\mathbf{x}_p - \mathbf{x}_q\|_2^2 \right) \quad (9)$$

where:

- ℓ is the free parameter for the length, or horizontal scale. It describes how quickly the correlation between two points drops as the distance between them increases. The higher it is, the smoother the sampled function is.
- σ_f^2 is the free parameter for the signal variance, or vertical scale. The higher it is, the greater the variation in the evaluation of sampled functions.

An example of a function sampled while varying the horizontal scale parameter ℓ is shown in figure 5. The plot shows that as ℓ increases the sampled function becomes smoother, while a very small value for ℓ results in a wiggly function. The shaded area shows the pointwise mean plus and minus two times the standard deviation for each input value, or else called the 95% confidence region.

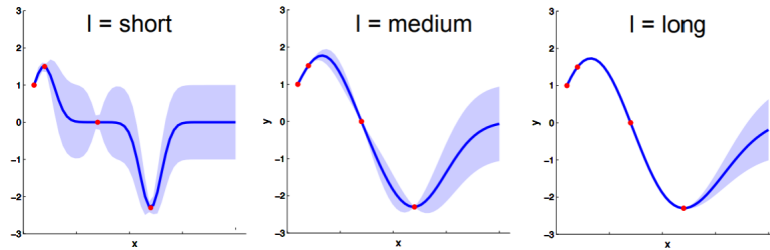


Figure 5. Gaussian process samples varying the length parameter ℓ . Image from Shi (2019).

Assuming that the observations $\mathbf{x}_{1:t}$, $\mathbf{f}_{1:t}$ are given from previous iterations, Bayesian optimization decides which point \mathbf{x}_{t+1} should be considered next. The value of the function at this arbitrary point is defined as $f_{t+1} = f(\mathbf{x}_{t+1})$, and because of the properties of GPs, $\mathbf{f}_{1:t}$ and f_{t+1} are jointly Gaussian (Frazier, 2018), as shown in formula 10.

$$\begin{bmatrix} \mathbf{f}_{1:t} \\ f_{t+1} \end{bmatrix} \sim \mathcal{N} \left(0, \begin{bmatrix} \mathbf{K} & \mathbf{k} \\ \mathbf{k}^T & k(\mathbf{x}_{t+1}, \mathbf{x}_{t+1}) \end{bmatrix} \right) \quad (10)$$

where:

$$\mathbf{k} = [k(\mathbf{x}_{t+1}, \mathbf{x}_1) \quad k(\mathbf{x}_{t+1}, \mathbf{x}_2) \quad \cdots \quad k(\mathbf{x}_{t+1}, \mathbf{x}_t)]$$

Importantly, there is a distinction between the posterior distribution and the predictive posterior distribution. The posterior distribution, shown in formula 3, represents the model’s belief about the unknown objective function conditioned on the observed data points and evaluations so far. On the other hand, the posterior predictive, shown in formula 11 (Brochu et al., 2010) is the distribution of possible values of f at unobserved data points \mathbf{x}_{t+1} , and is used to assess the model’s uncertainty about the function’s behavior in unexplored regions of the input space (Rasmussen & Williams, 2005). As such, it is crucial in determining which point to evaluate next, along with the acquisition function described in the following paragraphs.

$$P(y_{t+1}|\mathcal{D}_{1:t}, \mathbf{x}_{t+1}) = \mathcal{N}(\mu_t(\mathbf{x}_{t+1}), \sigma_t^2(\mathbf{x}_{t+1}) + \sigma_n^2) \quad (11)$$

where:

$$\begin{aligned} y_i &= f(\mathbf{x}_i) + \epsilon_i, \text{ which is the value of the function } f \text{ at point } x_i \text{ plus noise.} \\ \mu_t(\mathbf{x}_{t+1}) &= \mathbf{k}^T [\mathbf{K} + \sigma_n^2 I]^{-1} \mathbf{y}_{1:t}, \text{ which is the mean of the distribution.} \\ \sigma_t^2(\mathbf{x}_{t+1}) &= k(\mathbf{x}_{t+1}, \mathbf{x}_{t+1}) - \mathbf{k}^T [\mathbf{K} + \sigma_n^2 I]^{-1} \mathbf{k}, \text{ which is the covariance of the distribution.} \end{aligned}$$

The acquisition function, along with the posterior predictive distribution, is used to determine where to sample next in the parameter space, $\mathbf{x}_{t+1} \in A$ by trading off exploitation and exploration. Exploitation directs the search in the vicinity of the current best results, where $f(x)$ is optimal, while exploration directs the search in largely different areas in the parameter space that have not been probed yet (Frazier, 2018). Both methods correspond to high values for the acquisition function, so the goal is to maximize it to determine the next sampling point. Formally, the objective function f is sampled based on the formula in equation 12.

$$\mathbf{x}_{t+1} = \underset{\mathbf{x}}{\operatorname{argmax}} u(\mathbf{x}|\mathcal{D}_{1:t}) \quad (12)$$

where:

$$\begin{aligned} u &\text{ is the acquisition function.} \\ \mathcal{D}_{1:t} &= (\mathbf{x}_1, f(\mathbf{x}_1)), \dots, (\mathbf{x}_t, f(\mathbf{x}_t)), \text{ which are the } t \text{ samples drawn from } f \text{ so far.} \end{aligned}$$

There are several widely used acquisition functions, but their common trait is that they are defined in a way that high acquisition values correspond to potentially high values of the objective function. This can be because either exploitation or exploration is high, or both (Brochu et al., 2010). Besides determining the next sampling point, acquisition functions aim to minimize the number of objective function evaluations, since by definition black box functions are often expensive to evaluate. Additionally, acquisition functions usually do well even in settings where the objective function has multiple local maxima (Brochu et al., 2010).

As has been explained in the above paragraphs, the main components of Bayesian optimization are the posterior distribution over the objective function and the acquisition function. Using a GP to model the distribution over the objective function, the general outline of the algorithm is shown in algorithm 1. The algorithm starts with an initial, usually random vector \mathbf{x} representing the input variables and evaluates $f(\mathbf{x})$. At each iteration, the acquisition function is maximized to determine where to sample next from the objective function, as this is modelled with a GP. It thus takes into account the mean and variance of the posterior predictive distribution to explore the search space. After the value of the objective function y_{t+1} is sampled at the maximum of the acquisition

function, the Gaussian process is updated and the process is repeated, usually for a fixed and relatively small number of iterations (Brochu et al., 2010). In the end, the algorithm returns the values of the input vector \mathbf{x} that results in the minimum evaluation of the objective function. Bayesian optimization has the advantage of converging relatively quickly compared to other optimization algorithms, so a suggested number of iterations is around 30 (Brochu et al., 2010).

Algorithm 1 Bayesian optimization algorithm outline

1: Generate initial data \mathbf{x}_t with given constraints and evaluate $f(\mathbf{x}_t) = y_t$ such that

$$\mathcal{D}_t = \{\mathbf{x}_t, y_t\}$$

2: **for** $t = 1, 2, \dots$ **do**

3: Find \mathbf{x}_{t+1} by optimizing the acquisition function u over the GP such that

$$\mathbf{x}_{t+1} = \underset{\mathbf{x}}{\operatorname{argmax}} u(\mathbf{x}|\mathcal{D}_{1:t})$$

4: Evaluate the objective function, such that

$$y_{t+1} = f(\mathbf{x}_{t+1}) + \epsilon_{t+1}$$

5: Augment the data $\mathcal{D}_{1:t+1} = \{\mathcal{D}_{1:t}, (\mathbf{x}_{t+1}, y_{t+1})\}$

6: Update the GP posterior

7: **end for**

8: **return** $\mathbf{x}_{min} \in \mathcal{D}$

3 Methodology

Having provided the theoretical background of Bayesian optimization, the methodology section starts by describing how Bayesian optimization is used in this research for the optimal placement of multi-array brain electrodes. Sub-section 3.2 describes in detail the flow of the optimization pipeline, from the array configuration to modelling the phosphenes, while sub-section 4 describes the different experimental set-ups and how each one answers the corresponding research sub-question. The code for all parts of this research is openly available here.

3.1 Bayesian optimization for multi-array brain electrodes

In the context of electrode placement, the optimization procedure developed by van Hoof et al. (2024) calculates the optimal location and insertion angles of a single electrode-array. The procedure of this research was based on this implementation but was optimized and adapted for the inclusion of multiple arrays. The objective function f that is being minimized is a combination of different metrics for the difference between the target phosphene distribution and the predicted phosphene map inferred after placing the electrodes. The target phosphene distribution covers the entire visual field with appropriate spatial resolution, but realistically, it is impossible to obtain a full coverage of the visual field by stimulating neurons only in the V1 brain area. However, optimizing the procedure based on this ideal phosphene map effectively guides the optimization procedure towards finding the best possible parameters for maximal visual field coverage.

The four parameters of the objective function, captured by the vector \mathbf{x} and modelled with a Gaussian process, can be thought to belong into two categories. The parameters *alpha* and *beta*, describe the location in the brain where the array will be placed, while the parameters *shank length* and *shank offset* describe the design of the electrode array. As is described in more detail in section 3.2.2, *alpha* and *beta* refer to the angle of the virtually inserted implant, while *shank length* describes its cortical depth. In practice, this means that the larger the shank length, the greater the distance between the electrodes on the shank, since the distance, in mm, between the electrodes is defined as $\frac{\text{shank_length}}{n.\text{contact_points}-1\text{mm}}$. Additionally, the parameter *shank offset* describes the distance between the point where the electrode shank penetrates the cortex and the first contact point. For each new set of parameters, the resulting configuration can be either valid or invalid, depending on whether the contact points are located outside of the brain and whether the array overlaps with an already placed array.

Figure 6 illustrates some example placements for one electrode grid. The red grid serves as a reference and it is positioned at the initial location before the algorithm begins, at the center of the calcarine sulcus. The yellow grid indicates the virtually implanted position, and is calculated based on the *alpha* and *beta* parameters relative to the reference grid. Each placement can be either invalid 6b, or valid 6c, depending on whether the electrodes are outside of the grey matter or they overlap with another grid. When the virtual placement is invalid, a penalty term is added to the cost function to force the algorithm to learn to avoid such placements. More details about this are provided in the following paragraphs.

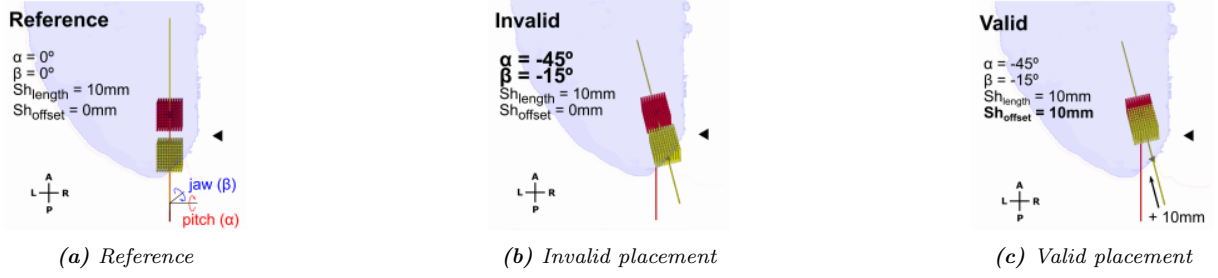


Figure 6. Example grid placement. The red grid is a reference array before the start of the algorithm, and the yellow grid indicates the virtually implanted position of the array. The parameters α and β indicate the position of the virtually implanted array relative to the reference array, while the parameters shank length and shank offset describe some aspects of the array design. Image from van Hoof et al. (2024, p. 4).

The algorithm minimizes a combination of three loss functions and finds the optimal configuration for the four parameters, resulting in the minimum difference between the target phosphene distribution and the predicted one after virtually placing the array. Informally, these loss functions consider the visual field coverage of the phosphene distribution (dice coefficient), the total number of validly placed electrodes on voxels within grey matter that generate a phosphene (yield), as well as the difference between the predicted phosphene density distribution and the desired one (Hellinger distance).

Formally, these loss functions are shown in the following formulas. The Sørensen-dice coefficient, shown in formula 13, is computed on two discretized sets of data, the binarized target phosphene map, TP , and the binarized predicted phosphene map, PP . Each map’s pixels are set to 1 if they contain phosphene activation and 0 if they do not, allowing the dice coefficient to obtain the phosphene maps that are localized in the desired visual region (van Hoof et al., 2024).

$$DC = \frac{2|TP \cap PP|}{|TP| + |PP|} \quad (13)$$

where:

$TP \cap PP$ is the conjunction of the target and the predicted phosphene maps.
 $|TP|$ and $|PP|$ represent the number of elements in each map.

The yield loss function is defined with formula 14, reflecting the ratio between the total number of validly placed electrodes within grey matter voxels that can yield a phosphene over the total number of contact points on the array. This allows to reward solutions that can yield the maximum number of phosphenes (van Hoof et al., 2024).

$$Y = \frac{\text{number of hits}}{\text{total number of contact points}} \quad (14)$$

The Hellinger distance, shown in equation 15, is a measure of dissimilarity between two probability distributions. It is restricted in the range between 0 and 1 and it is often used in machine learning to compare two normalized discrete probability distributions. The maximum distance between the two distributions, 1, is achieved when one distribution assigns a probability of 0 to every set where the other distribution assigns a positive probability, and vice versa. As such, Hellinger distance rewards configurations for which the virtually implanted electrodes yield a phosphene map with the desired density distribution, while penalizing density distributions diverging from the target distribution.

Phosphene density is an important element since it is crucial for pattern recognition and recognition of objects.

$$H(P, Q) = \sqrt{\sum (\sqrt{P} - \sqrt{Q})^2} \quad (15)$$

where:

- P is the phosphene map with the predicted density distribution.
- Q is the phosphene map with the target density distribution.

As mentioned previously, the algorithm doesn't consider these loss functions individually, but instead it minimizes their linearly weighted combination, as shown in equation 16. The weights can be chosen to value one aspect of the loss over another and could be themselves optimized, but in this implementation, emphasis was given primarily to the contribution of the visual field coverage (DC) and the phosphene distribution (H), by a factor of 20 relative to the number of phosphene-evoking electrodes (Y). This is because the interest in this research is to maximize the similarity between the target and the predicted phosphene map regardless of the number of phosphene-evoking electrodes. Favouring these two terms by a factor of 20 relative to the yield allows the algorithm to quickly learn that yield should have less influence in driving the optimization, relative to the other terms. As such, the parameters a and c were set to 1, while the parameter b was set to 0.05. These values were determined experimentally for this implementation by comparing the results of the algorithm for different values of the c parameter. Specifically, the values that were tested were 0.1, 0.05, and 0.01. The weight parameters can of course be adapted to favour one term of the loss function over another based on the desired outcome.

Additionally, a penalty was added to the loss function to force the algorithm to avoid invalidly placed arrays. Specifically, an array is considered invalid if any part of it is outside the grey matter area, or if it overlaps with another array that is already virtually placed (in the case of multiple arrays). The penalty of 0.75 reflects an addition of 0.25 to each of the three terms of the loss function, and it is the same regardless of the reason that makes the array invalid. This means that the algorithm learns to avoid invalid placements in the same way, regardless of whether the placement is invalid because it is outside grey matter or because of overlap with another array. Without the penalty term, the cost function can have a maximum value of 3 in the worst case, so an addition of 0.75 is an addition of 25% relative to the worst case, which allows the algorithm to quickly learn to avoid invalid placements.

$$Loss = \begin{cases} (1 - aDC) + (1 - bY) + cH, & \text{if array is valid} \\ (1 - aDC) + (1 - bY) + cH + 0.75 & \text{if array is invalid} \end{cases} \quad (16)$$

where:

- a is the weight of the dice coefficient.
- b is the weight of the yield.
- c is the weight of the Hellinger distance.

The inclusion of multiple arrays aims to increase the overall visual field coverage and the density distribution of the generated phosphenes. As such, when optimizing each additional array, the loss function considers the dice coefficient and the Hellinger distance

of the phosphene map that is generated by all implanted arrays so far. On the other hand, the yield loss considers the number of phosphene evoking electrodes of the array that is being optimized at the moment, not the combined yield.

For the implementation of the optimization procedure, the package `scikit-optimize` (2024) is used in Python 3.11 (Van Rossum & Drake, 2009). The objective function is modelled with a Gaussian process as a surrogate model, and thus it is minimized with the package’s function `gp_minimize`. The Gaussian process is initialized with 10 points in the parameter space that are generated with Latin Hypercube Sampling using the maximin criterion. Afterwards, for every iteration of the Bayesian optimization algorithm, the Gaussian process is used to optimize the acquisition function, suggesting the next point to evaluate. The objective function is then evaluated at this point and the Gaussian process model is updated. In this implementation, the acquisition function was probabilistically chosen at every iteration, varying among the lower confidence bound, the negative expected improvement, and the negative probability of improvement (scikit-optimize, 2024).

This procedure was repeated for every array, with the constraints that each array must not be positioned outside grey matter, and it must not overlap with an existing array. As such the optimization algorithm has the following form:

Algorithm 2 Bayesian optimization for multi-array brain electrodes

```

1: optimized_parameters  $\leftarrow$  empty dictionary
2: for array = 1, 2, ... do
3:   Generate initial data  $\mathbf{x}_t$  in the parameter space using Latin Hypercube Sampling
4:   and evaluate  $f(\mathbf{x}_t) = y_t$  such that

$$\mathcal{D}_t = \{\mathbf{x}_t, y_t\}$$

5:   for  $t = 1, 2, \dots$  do
6:     Find  $\mathbf{x}_{t+1}$  by optimizing the probabilistically chosen acquisition function  $u$  over
7:     the GP such that

$$\mathbf{x}_{t+1} = \underset{\mathbf{x}}{\operatorname{argmax}} u(\mathbf{x}|\mathcal{D}_{1:t})$$

8:     Evaluate the objective function, such that

$$y_{t+1} = f(\mathbf{x}_{t+1})$$

9:     Augment the data  $\mathcal{D}_{1:t+1} = \{\mathcal{D}_{1:t}, (\mathbf{x}_{t+1}, y_{t+1})\}$ 
10:    Update the GP posterior
11:  end for
12:  if array is valid then
13:    optimized_parametersarray  $\leftarrow \mathbf{x}_{min} \in \mathcal{D}$ 
14:  else
15:    continue
16:  end if
17: end for
18: return optimized_parameters
```

This procedure is implemented twice for each subject, once on each hemisphere of the brain, since the implementation considers the visual field of each hemisphere and

the array implantation procedure separately. Additionally, even though this procedure may be used for an arbitrary number of electrode arrays, for example 5, it may end up finding a valid configuration for a smaller number, for example 4. This can be because the algorithm did not find a valid brain location where the next array can be placed that decreases the loss function.

3.2 Flow of the optimization pipeline

Figure 7 shows a diagram of the virtual multi-array electrode placement pipeline. White shapes indicate processing steps, the light blue shapes indicate the parts of the Bayesian optimization procedure, while the diamond shapes indicate evaluation checks necessary to ensure the robustness of the procedure. The following sub-sections explain each of these steps in detail, substantiating important modelling choices.

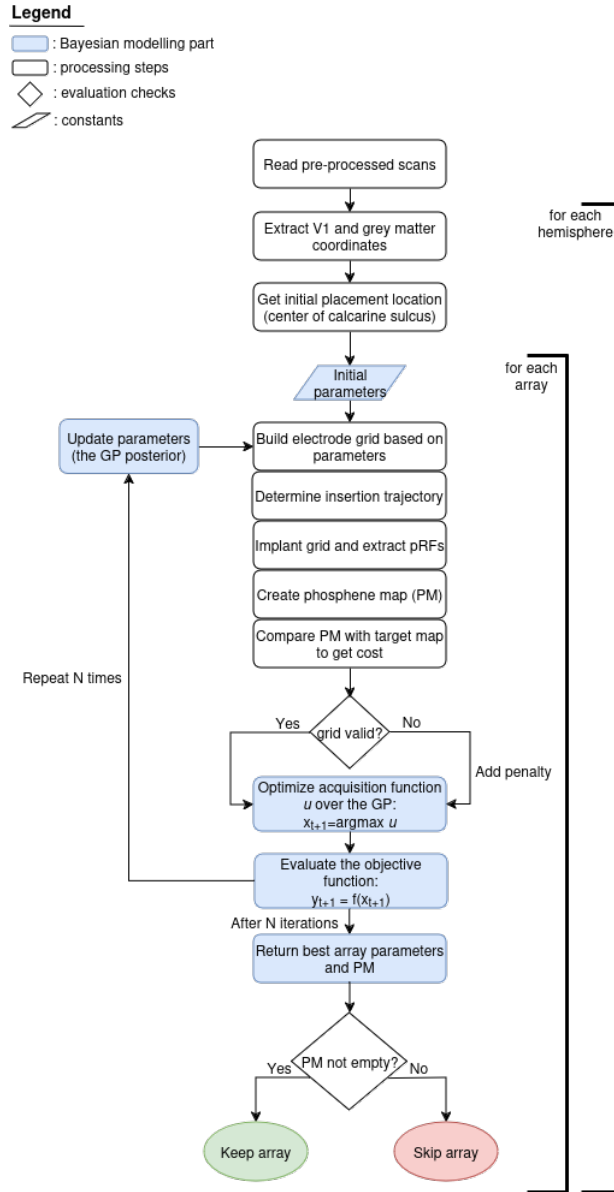


Figure 7. Overview of virtual multi-array electrode placement pipeline.

3.2.1 Dataset and extraction of relevant brain coordinates

Similarly to the procedure by van Hoof et al. (2024), the optimization pipeline made use of anatomical and retinotopy data from the Human Connectome Project 7 Tesla retinotopy dataset (Benson et al., 2018). The structural T1-weighted and T2-weighted MRI scans have a $0.7mm$ isotropic resolution and were not pre-processed anew, but they were used after having been pre-processed by van Hoof et al. (2024). The relevant brain coordinates, including the V1 area, the grey matter, and the calcarine sulcus, were extracted using Freesurfer’s cortical parcellation and the Desikan-Killiany atlas, as well as the maps provided by Benson et al. (2018). These were then used to guide the optimization procedure by estimating the population receptive field maps (pRFs) and the phosphene locations, as is described in the following sections.

Importantly, the resolution of the retinotopy data plays a critical role in the estimation of the phosphene map, because it determines the simulated visual field coverage. An isotropic resolution of $1mm$ means that the voxel size has a volume of $(1mm)^3$, and if two electrodes are virtually implanted within that voxel their simulated phosphenes would be identical. As such, scans with a higher resolution, ie. a smaller voxel size, allow for a more accurate estimation of the phosphene map, especially when considering a smaller distance between the electrodes. As will explained in the following sections, this bears significant importance especially when considering the simulation of the Utah array in experiment 3, in 4.3, where the distance between the electrodes is $0.4mm$.

To accelerate the optimization procedure, the center of the calcarine sulcus was selected as an initial sampling point, since it is a reliable estimate of the location and total volume of the V1 brain area (van Hoof et al., 2024). The initial grid location was the centroid, or the geometric center, of the calcarine sulcus, which was calculated using the medians along the three dimensions of its total volume. The grid was virtually implanted there with initial parameters *alpha*: 0° , *beta*: 0° , *shank offset*: $25mm$, and *shank length*: $10mm$.

3.2.2 Build and virtually implant grid based on insertion trajectory

The first step of each iteration in the optimization pipeline is to build the virtual electrode grid. This takes into account the parameter *shank length*, which as mentioned in section 3.1, determines the distance between the electrodes on each shank. Afterwards, the electrode grid is virtually placed on the modelled brain, based on the parameters *alpha* and *beta* which define the insertion trajectory of the grid, and the parameter *shank offset*, which determines the distance between the insertion point on the cortical surface and the first contact point on the electrode shank. Figure 8 shows an example of the grid’s configuration parameters in 8a, and a simulated placement in the V1 area of the brain in 8b. The space between the shanks is shown to be $1mm$ here, but this differs depending on the research question being explored, as is discussed in section 4.



Figure 8. Illustration of electrode grid configuration (8a) and placement (8b) van Hoof et al. (2024, p. 4).

Table 1 shows an overview of the range of the parameters, as well as their initial values. The parameter *alpha*, or pitch, defines the rotation of the grid around its lateral axis, and it was set to vary between -90° and 90° degrees, allowing to cover a total range of 180° . A wider range would be redundant since the additional angles would be a duplicate orientation due to the periodicity of rotations, and it would also mean approaching a location from within the brain, which is of course impossible. The parameter *beta*, or yaw, defines the rotation of the grid around its vertical axis, and it was set to vary per hemisphere to avoid contact with the other hemisphere. Specifically, *beta* was set to range between -15° and 110° for the left hemisphere and between -110° and 15° for the right hemisphere. Roll, or *z*, defines the rotation of the grid around its longitudinal axis, but there was no need to vary it so it was always set to 0° when virtually implanting the grid.

Parameter	Value range	Initial value
alpha	$[-90^\circ, 90^\circ]$	0°
beta	LH: $[-15^\circ, 110^\circ]$, RH: $[-110^\circ, 15^\circ]$	0°
shank offset	$[0mm, 40mm]$	$25mm$
shank length	$[10mm, 20mm]$	$10mm$

Table 1. Overview of parameters' range and their initial values.

The parameter *offset from base* was set to range between $0mm$ and $40mm$, while the parameter *shank length* was set to range between $10mm$ and $20mm$ when exploring sub-questions 1 and 2, as mentioned in section 1.2, allowing for a distance between the electrodes on the shank in the range of $1.11mm$ and $2.22mm$. Sub-question 3 explores the implementation of the Utah array, as described by Blackrock-Neurotech (2024) and Zardini et al. (2021), which has a fixed design with a specific distance between the electrodes. As such, for sub-question 3, the shank length was not included as a parameter to be optimized, and was fixed at $3.6mm$, thus defining the distance between the electrodes at $0.4mm$. To facilitate the simulation in this case, the shank length does not describe the length of a shank with a single electrode, but a row in the two-dimensional array with 10 electrodes, as will be explained in section 4.3

Even though this configuration allows to implement the optimization procedure for a widely used array design, the generated phosphene map is underestimated due to the $1mm$ isotropic resolution of the retinotopy data. As was mentioned above in section 3.2.1, if two electrodes fall within the same voxel, the simulated phosphenes will be identical. Since the distance between the electrodes of the Utah array is $0.4mm$, a lot of electrodes will fall in the same voxel, resulting in simulating less phosphenes than would be allowed with a higher resolution.

3.2.3 Extract pRFs and create phosphene map

The retinotopic data provided by Benson et al. (2018) allow to infer the population receptive field (pRF) maps. These describe the location and the size of the receptive field for each 1mm isotropic voxel, and are called *population* RF maps because there are several neural cells in a single 1mm voxel for which the response is being measured. For this work, the pRF maps were provided by van Hoof et al. (2024), and were computed with the following procedure. Firstly, Freesurfer’s *mri_surf2surf* function was used to warp the pRF surface maps based on empirical data in Freesurfer fsaverage space to individual space. Then, the inference of the retinotopic maps is done with Neuropythy’s *register_retinotopy* command, which harmonizes the anatomical inference of the pRF maps, the atlas described by Benson et al. (2014), and the experimental retinotopy data (Benson et al., 2018) comprised of retinotopic responses to visual stimuli up to 8 degrees eccentricity (van Hoof et al., 2024).

The predicted phosphene map is created based on the electrode coordinates and the matching voxels of the retinotopic map. Specifically, each individual electrode intersecting a voxel in the retinotopic map yields a phosphene on a 1000-by-1000-pixel image grid, scaled by a maximum eccentricity, aka as view angle, of 90° . Additionally, the spread of the stimulation current to the voxel size of the retinotopic map is fixed at 1mm^3 . The phosphenes are modelled as two-dimensional Gaussian circular spots of light with standard deviation ranging from 0.2 up to 3 visual degrees, depending on the receptive field size as scaled by eccentricity (Tehovnik, Slocum, Carvey, & Schiller, 2005) and a simulated stimulation amplitude of 100 micro-amps (van Hoof et al., 2024). Figure 9 shows an example of a predicted phosphene map where the maximum eccentricity, or degree of visual angle (dva), is a little bit over 30, and the color codes for eccentricity.

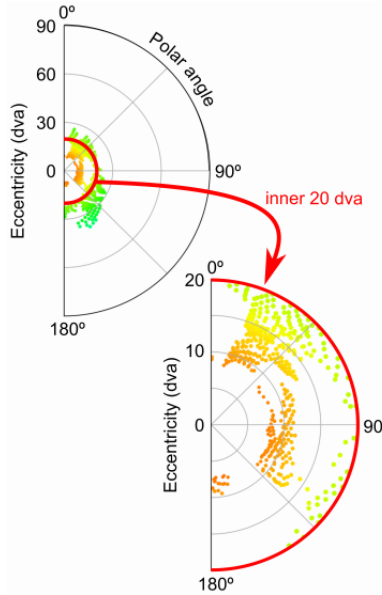


Figure 9. Example of a predicted phosphene map, where color codes for eccentricity. Image from van Hoof et al. (2024, p. 4).

3.2.4 Compare predicted phosphene map with the target map and get cost

Having virtually implanted the electrode array based on the corresponding parameters and estimated the predicted phosphene map, the next step is to compare this pre-

dicted map to the target map using the loss function described with formula 16. The higher the value of the loss function, the greater the difference between the predicted map and the target map, so the optimization algorithm tries to maximize the similarity between the two maps, by minimizing the loss function. Figure 10a shows a target map on the left that covers the entire right hemifield, and the predicted map on the right, after having placed the electrode array.

As mentioned in section 2.1, cortical magnification allows to have a more detailed representation of the central part of the visual field compared to the peripheral part. This is because there is a higher density of neurons devoted to processing information from the central part of the visual field, allowing for finer spatial discrimination around the fixation point. When representing the visual field with phosphenes, a higher density is reflected in the number of overlapping phosphenes. In this work, phosphene density was modelled with a probability density function (PDF) of the phosphene map, and was computed with Gaussian kernel density estimation using the SciPy library (Virtanen et al., 2020).

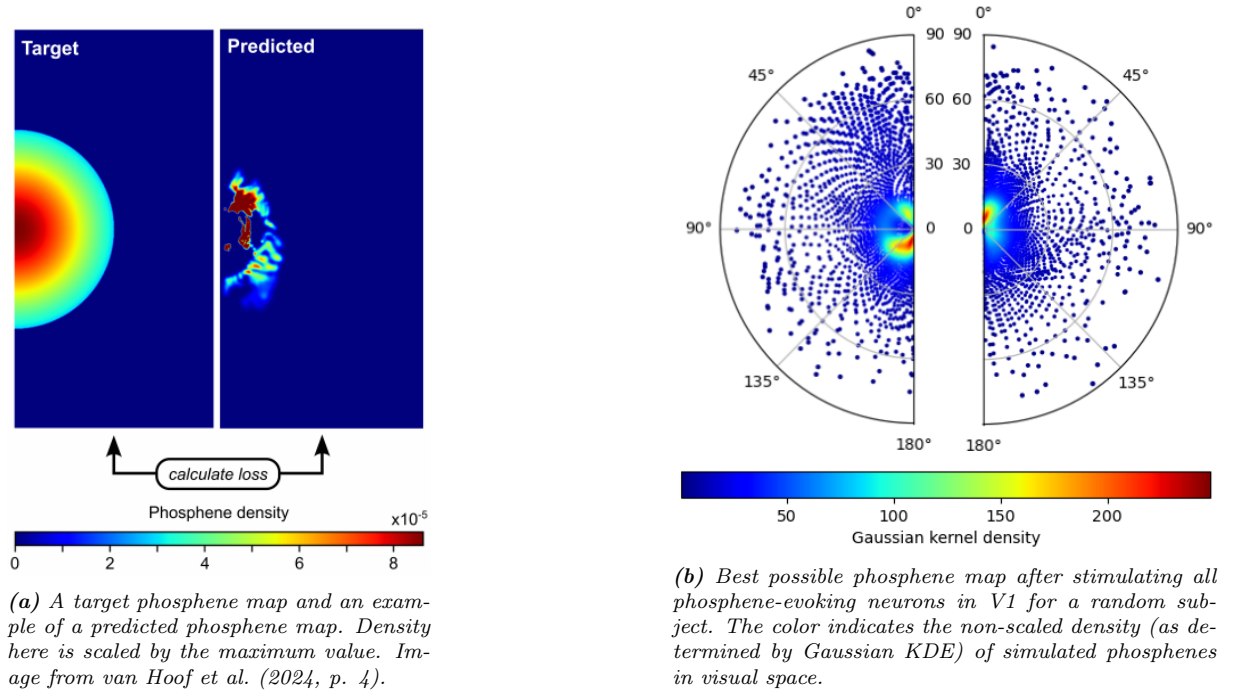


Figure 10. Illustration of an example phosphene map with the target map (10a), and the best possible phosphene map that could theoretically be generated (10b).

As shown on the target map in 10a, and as mentioned in section 3.1, it is impossible to obtain a full visual field coverage by stimulating voxels only in the V1 brain area. An example of the best visual field coverage for a random subject is shown on figure 10b, where the phosphenes are generated after stimulating all phosphene-evoking voxels in V1. Importantly, with the current electrode array designs and the constraints of the surgical procedure, it is impossible to stimulate all phosphene-evoking voxels. Therefore, since there is a limit to the amount of visual field coverage that can be achieved, and since patients may have different functional needs, it is important to be able to drive the array placement in a way that targets a specific sub-region of the visual field. This allows to also check whether the algorithm indeed optimizes the visual field coverage towards the target map. Therefore, the optimization procedure was tested to target four distinct target coverages, which allowing to test whether the algorithm actually optimizes a target

area instead of any specific large coverage (van Hoof et al., 2024):

1. *Full target*: dense representation starting from the fovea, reaching a maximum of 90° eccentricity.
2. *Inner target*: dense representation starting from the fovea, reaching a maximum of 45° eccentricity.
3. *Upper target*: dense representation around the fovea, reaching a maximum of 90° eccentricity and a maximum of 45° polar angle to cover the upper visual field.
4. *Lower target*: dense representation around the fovea, reaching a maximum of 90° eccentricity, and polar angles between 135° and 180° to target the lower visual field.

Table 2 shows the resulted phosphenes after applying the optimization procedure in V1 brain area on a random subject for each of the four target regions. As was mentioned in section 2.2, stimulating neurons in one hemisphere yields phosphenes in the contralateral visual field. The visualizations confirm that indeed the majority of the phosphenes and the highest density fall within the target coverage, although there are some phosphenes outside that area. The procedure here was implemented with five three-dimensional arrays of shape $10 \times 10 \times 10$, and the valid arrays across all eight runs were between three and five. As mentioned previously, after the completion of the optimization procedure, some arrays may still be invalidly placed or yield no phosphenes, so in that case they are disregarded.

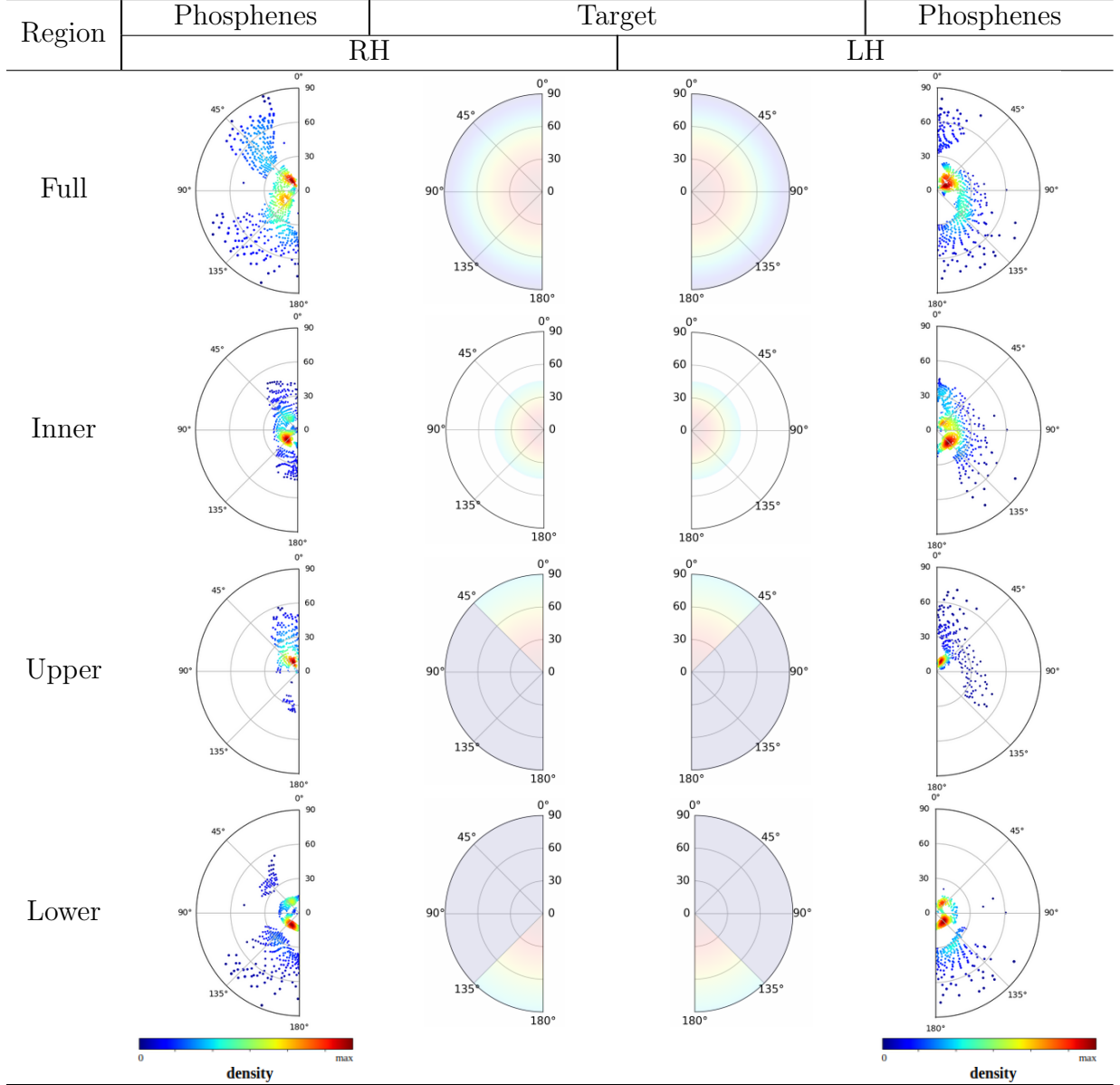


Table 2. Target visual field coverage and corresponding generated phosphenes after applying the optimization procedure in V1 brain area for a random subject. The color indicates the density (as determined by Gaussian KDE) of simulated phosphenes in visual space.

3.2.5 Evaluate the grid’s validity

At each iteration of the optimization cycle, the grid is evaluated about whether it falls outside the grey matter area and whether it overlaps with an already placed array. If any of these conditions are true, a penalty is added to the loss function, as described in formula 16, to force the algorithm to avoid the parameters that result in that placement. Computationally, estimating whether the grid falls within the grey matter area of the brain is done by converting the three-dimensional grey matter coordinates to a point-cloud and then taking its convex hull, using the trimesh library (Dawson-Haggerty et al., 2024). Then if there is any contact point in the grid that is not within the grey matter convex hull, the grid is consider invalid.

For evaluating the overlap with an already placed array, the procedure depends on the array configuration. In the case of a three-dimensional array, as is implemented for

sub-questions 1 and 2, the computations are similar. Having determined the current grid location, each previously placed three-dimensional array is transformed into a convex hull, and if any coordinate of the current grid is within the convex hull of any already placed array, the current grid is considered invalid. For sub-question 3, the goal is to use a widely used array design, which is essentially two-dimensional, of shape $1 \times 10 \times 10$. Additionally, to inform realistic clinical or research applications it is informative to be able to specify the desired distance between the arrays, so that the surgical constraints are taken into account. For these reasons, the computations to estimate overlap among the arrays is different. Firstly, having determined the current grid location, the minimum distance between the coordinates of the current grid and each already placed grid is estimated. Then if that distance is smaller than the minimum desired distance between the arrays, the current grid is considered invalid. As is described in section 4, the minimum distance between the arrays for sub-question 3 was set to $1.5mm$.

At the end of the optimization procedure for each array, the array is evaluated again to make sure that the resulted placement produces a phosphene map. This evaluation is required because as the pipeline progresses to more arrays, it can be the case that a valid placement within V1 hits no phosphene evoking voxels due to the existence of the other arrays. In such a case, the procedure disregards that array, and it necessarily results in the placement of less than the specified number of arrays.

4 Experiments

The pipeline developed for this research offers a generic solution for many clinical and research settings that require a virtual implantation optimization. This section explores the three specific research questions, as they were mentioned in section 1.2. Each sub-section describes the experimental set-up for each research question, presents the results, and provides a small experiment-specific discussion. A general discussion is presented in section 5.

Each set up was easily adapted by changing the configuration file of the pipeline, defining all relevant variables for the array dimensions, and the optimization parameters. All experiments were run using the anatomical and retinotopy data of 181 subjects from the Human Connectome Project 7 Tesla retinotopy dataset (Benson et al., 2018) and targeting the full visual field, as described in section 3.2.4. Additionally, the initial parameters were the same for all set ups, specifically *alpha*: 0° , *beta*: 0° , *shank offset*: $25mm$, and *shank length*: $10mm$. As will be explained when describing the third experiment in 4.3, the *shank length* was not included as a parameter in this set up and was fixed at $3.6mm$.

To accelerate the collection of the experimental data, each set up made use of multi-processing. The framework that was used was Ray (Ray team, 2024), and the multi-processing configuration made use of all 8 performance cores in the system’s CPU, distributing the collection of data to 8 workers. Each worker was devoted to one subject, thus allowing to run independent processes in parallel. The CPU was an Intel Core i7-12700H of generation 12. Importantly, all set ups were run locally on a commodity laptop, so even though using a cloud environment or a high-performance computing cluster would accelerate the procedure, it is not necessary.

4.1 Experiment 1: Multiple 3d arrays vs one, based on individual scans

4.1.1 Experimental set-up and analysis

The first sub-question explores the benefit of using multiple three-dimensional arrays compared to using only one three-dimensional array. It also allows to explore the added benefit of each individual array, thus making it possible to infer when additional arrays barely improve the result. This could help select the optimum number of arrays for a given application. For this experiment in particular, the number of arrays was set to 5, but it can easily be configured for an arbitrary number of arrays by only changing the relevant variable in the config file. The procedure optimizes the array placement parameters (*alpha*, and *beta*), as well as some aspects of the array design (*shank length*, and *shank offset*) based on individual anatomical scans. Then, the resulted phosphene map is compared to the phosphene map after having implemented only 1 array. As was mentioned in section 3.2.5, it can be the case that the total number of arrays is smaller than 5, because the procedure could not find a valid placement for the last array(s) that yields a phosphene map.

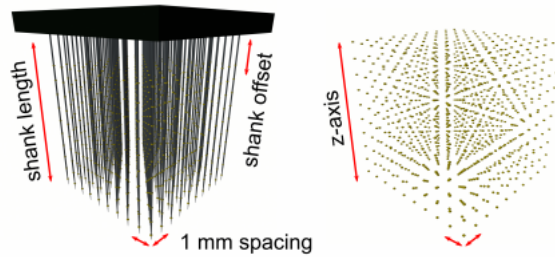


Figure 11. Example grid of shape 10x10x10. Image from van Hoof et al. (2024, p. 4).

The array configuration was the same as the one implemented by van Hoof et al. (2024), with a shape of 10x10x10, meaning that there were 10 lines of 10 shanks, with each shank having 10 stimulating electrodes, giving a total of 1000 electrodes. An example of such an electrode array is shown in figure 11, where the distance between the shanks is 1mm. The optimization ran for 150 iterations for each array, and returned the best optimization parameters for the placement of each array, for each hemisphere, and for each of the 181 subjects.

Since the optimization procedure was applied independently to each hemisphere, results were analyzed using one repeated measures ANOVA per hemisphere with the number of arrays as independent and within-factor variable. This allows to infer whether the inclusion of several arrays in each hemisphere makes the predicted phosphene map more similar to the desired target phosphene map. This is evaluated by evaluating whether the number of arrays has a statistically significant effect on the cost function, as described in formula 16. The significance level of 0.05 was Bonferroni-corrected for multiple comparisons. Subsequently, for each hemisphere, post-hoc pairwise comparisons were conducted with Tukey’s honestly significant difference (HSD) test to investigate the influence of each array on the cost compared to each other array. Tukey’s HSD method was preferred because it allows to control the family-wise error rate across any number of pair-wise comparisons (Greenwood, 2022). This means that the overall rate of at least one Type I error across all tests remains at the specified significance level of 0.05. All tests and

statistical assumptions were conducted using the Python library statsmodels (Seabold & Perktold, 2010).

4.1.2 Results

Having completed the optimization pipeline for the placement of 5 arrays, the resulting phosphene map can be estimated. As was mentioned in section 3.1, it is possible that the procedure terminates without finding a placement for all 5 arrays because there is no valid placement within V1 that yields a phosphene map. Figure 12 shows a binarized version of the phosphene map per hemisphere and array, while figure 13 shows the estimated density per hemisphere after placing all arrays for an example subject, 552241.

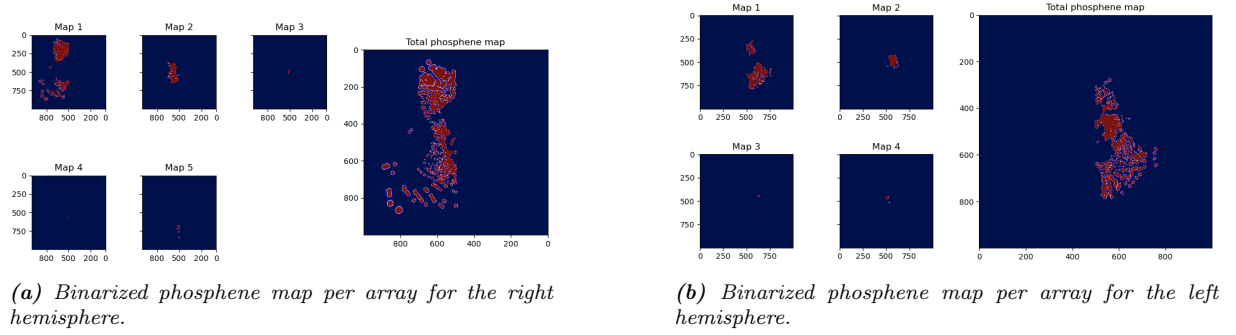


Figure 12. Binarized phosphene maps per hemisphere and array, for subject 552241.

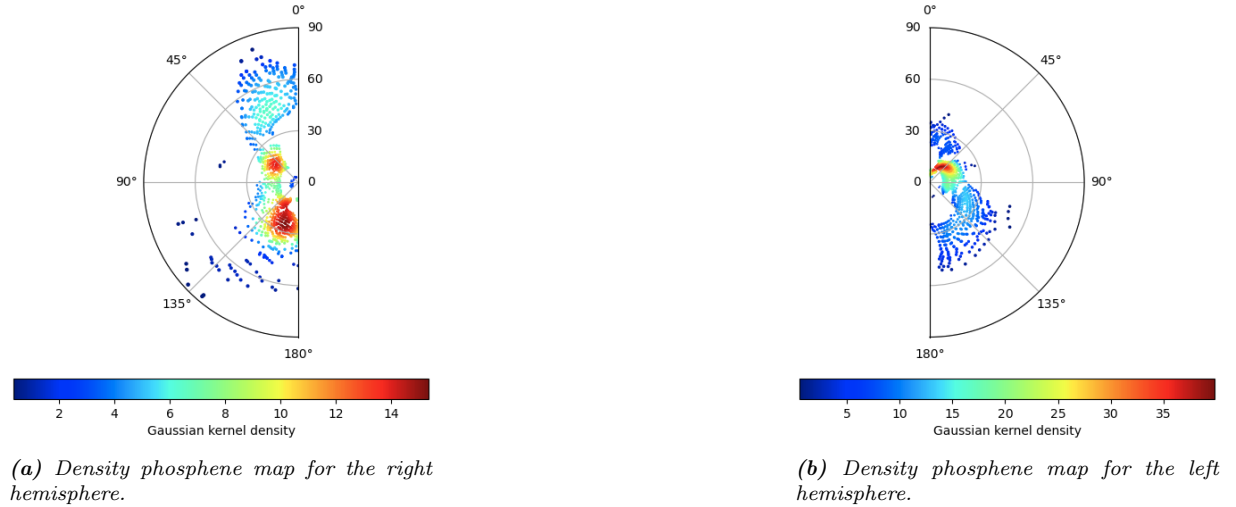


Figure 13. Density phosphene map based on all arrays per hemisphere, for subject 552241.

Figure 14 shows the mean total cost as estimated using formula 16, as well as its individual components, as described in section 3.1. The figure shows the cumulative average values, and their 95% confidence interval, for each loss component based on the total number of subjects for which the optimization procedure completed all 5 arrays. For example, the cumulative average cost at array 3 is 2.25, and represents the total estimated cost after having placed arrays 1, 2, and 3. The procedure completed the placements of 5 arrays for 116 subjects for the left hemisphere and 106 for the right.

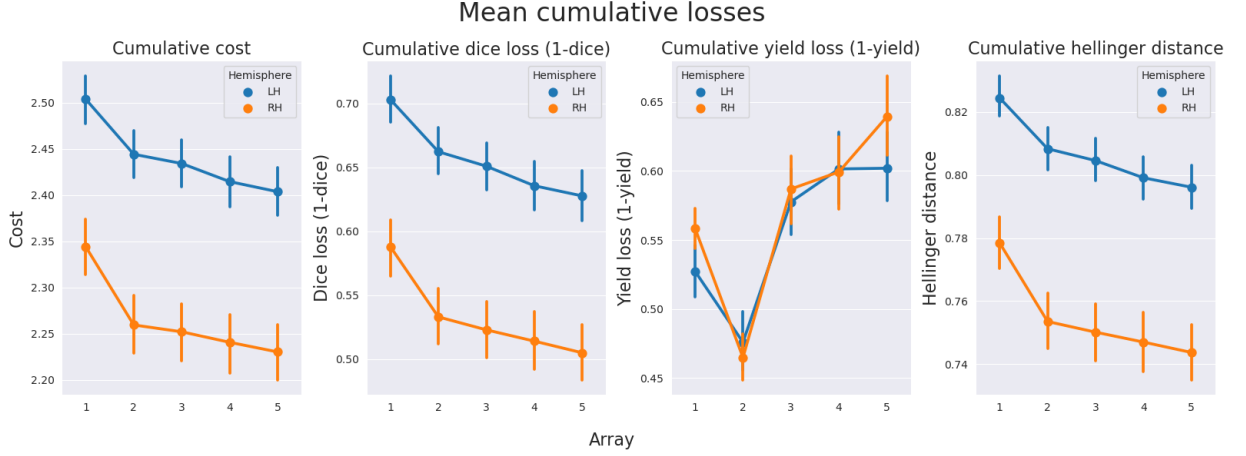


Figure 14. Mean cumulative losses per array. The error bars indicate a 95% confidence interval around the mean value. This means that across hypothetical repeated samples, the mean value will fall within the range of the error bars 95% of the time.

The visualization shows a big decrease in the cost function when comparing the first and the second array, and smaller but steady decrease for each additional array. Descriptive results per hemisphere for the linearly weighted cost function, as well as for each individual parameter are shown in the appendix section, on table 7. To infer whether the inclusion of additional arrays has a statistically significant impact on the cost per hemisphere, one repeated measures ANOVA was conducted on the data of each hemisphere, of all subjects for which the procedure completed the placement of 5 arrays. The results are shown in table 3. The necessary assumptions for a repeated measures ANOVA were met and are provided in the appendix section A.2.

Hemisphere	Subs completed	Factor	F value	DoF num.	DoF denom.	p-value
LH	116	n. of arrays	78.3952	4	460	< 0.0001
RH	106	n. of arrays	155.8899	4	420	< 0.0001

Table 3. Results of repeated measures ANOVA on data from each hemisphere.

Results showed that the inclusion of multiple arrays had a statistically significant impact on the cost function, both for the left $F(4, 460) = 78.4$, $p < 0.0001$, and the right hemisphere $F(4, 420) = 155.89$, $p < 0.0001$.

To investigate the effect of each array on the cost function per hemisphere, pairwise comparisons were run with post-hoc Tukey's HSD test. As was mentioned in section 4.1.1, this method inherently controls the family-wise error rate at the specified significance level across any number of pair-wise comparisons (Greenwood, 2022). For the left hemisphere, the mean cost function was significantly larger between the first and the second array ($M = 0.0596$, $SD = 0.037$) between the first and the third ($M = 0.0696$, $SD = 0.0551$), the first and the fourth ($M = 0.0892$, $SD = 0.0835$), and the first and the fifth ($M = 0.1001$, $SD = 0.0851$). In a similar manner, for the right hemisphere, the mean cost function was significantly larger between the first and the second array ($M = 0.0846$, $SD = 0.047$, the first and the third ($M = 0.092$, $SD = 0.0641$), the first and the fourth ($M = 0.1034$, $SD = 0.0707$), as well as the first and the fifth ($M = 0.1138$, $SD = 0.0777$). The remaining pairwise differences for the cost function between the additional array pairs were not statistically significant for either hemisphere. Table 9 shows all pairwise comparisons in the appendix section A.3.

4.1.3 Discussion

The aim of the first experiment was to explore the benefit in visual field coverage of using multiple three-dimensional arrays compared to using only one such array. The optimization procedure was performed for 5 arrays with a hypothetical array design of shape 10x10x10, allowing to vary some of the array parameters, as described in section 3.2.2. The results in section 4.1.2 show that there is a continuous and statistically significant decrease in the cost function when comparing the cost of each additional array to the cost of the first array. As becomes apparent from figure 14, the magnitude of the benefit on the cost function becomes smaller with the placement of each additional array, with the biggest impact gained from adding the second array. Research and clinical applications could take this into account when designing a procedure with multiple arrays.

However, one should take into account that this three-dimensional array already contains a large amount of electrodes, namely 1000 each. This is much more than the electrode count that is currently used in clinical experiments (Fernández et al., 2021), or even animal research (Chen et al., 2023). When implementing an array with fewer electrodes, it is likely that the benefit of including more arrays will not decline so much, as will be explored in the third sub-question in 4.3.

As is visible from the same figure, 14, the decrease in the cost function is driven primarily by the dice and the Hellinger distance losses, which continuously decrease, while the yield loss progressively increases after the second array. This is an expected result, since the cost function was heavily weighted on the dice and the Hellinger distance loss with a factor of 20 relative to the yield loss. These weights can be easily adapted based on the goals of the application, thus choosing to favor one aspect of visual field coverage over another.

The fact that each additional array decreases the cost progressively less can be explained by the greedy nature of the algorithm. A greedy algorithm approaches problem-solving with the heuristic of making the locally optimal choice at each stage, which may not find the globally optimal solution (Black, 2022). In this case, the array location and design is optimized for each array serially, so the optimal configuration for the first array may result in parameters for the next arrays that are sub-optimal in terms of the overall cost function. For example, if a wider shank length was found to be optimal for the first array, that means that any additional arrays cannot be placed in the same physical space, which apparently yields a high visual field coverage since it was the best location for the first array. Future research could address this issue by developing more complex optimization procedures that could, for example, retrospectively adapt the location and the configuration of the already placed arrays.

Additionally, the procedure also reveals a stable lateralization effect, showing that the visual field coverage is substantially higher for the right hemisphere (ie. the left visual field), compared to the left hemisphere (ie. the right visual field). Currently, it is unclear what is the cause of this difference. It would be interesting for a future implementation to explore whether this is due to inherent anatomical factors, the accuracy of the retinotopy dataset that was used (Benson et al., 2018), or perhaps it could be decreased by adjusting the cost function for each hemisphere separately. To exclude that this is a by-product of the optimization algorithm, one could mirror all the right hemispheres and explore whether this makes the results more similar to the left hemisphere. If after mirroring the results for the right hemisphere are still not similar to the ones for the left hemisphere, then it is likely something intrinsic to the retinotopy or the anatomical data.

4.2 Experiment 2: Multiple 3d arrays based on individual scans vs multiple 3d arrays based on the average brain scan

4.2.1 Experimental set-up and analysis

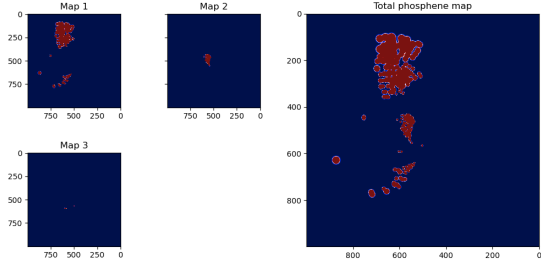
The second sub-question explores the benefit of using individual anatomical scans to determine the optimal array location, compared to using Freesurfer’s average brain. Given that the optimization pipeline is costly, both in terms of computation and time, there is no point in using the individual anatomical scans if there is not a significant improvement in the phosphene map as compared to the phosphene map using the average brain scan.

Thus, to explore the benefit of using the individual scans, this experiment compares the phosphene maps as they were generated by the procedure in experiment 1 in section 4.1, to the phosphene maps generated by optimizing the placement in the average brain. This was done by running the procedure once on Freesurfer’s average brain and returning the optimized parameters for the placement of the array. Afterwards, the array was built based on these parameters, and virtually implanted on all 181 subjects by reading their anatomical scans, to get the resulted phosphene map. This procedure was substantially less time consuming, since the most timely expensive part of the procedure is the optimization, and in this case the optimization was implemented only once per hemisphere, for the average brain. The array configuration and the parameters were identical to the ones described in experiment 1 in section 4.1.

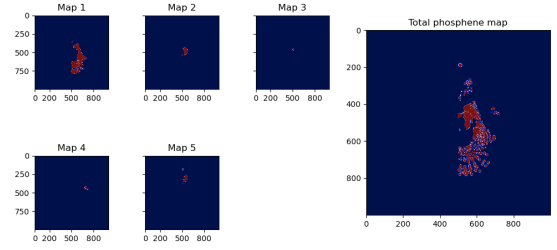
In a similar fashion to the analysis in experiment 1, in section 4.1.1, the results were analyzed per hemisphere, using a paired samples t-test, and using Bonferroni correction to adjust the significance level for multiple comparisons. The paired samples t-test was selected because the independent variable in this experiment is the methodology, which has two levels: individualized and average. All 181 subjects were compared on the basis of the last validly placed array, and the hypothesis was that the individualized approach will result in a lower cost function compared to the average. The statistics were performed using the Python library SciPy (Virtanen et al., 2020).

4.2.2 Results

The pipeline using the average approach places each array in the brain of all individuals using the same best parameters found from running the optimization on the average brain. Figure 15 shows the resulting phosphene map per hemisphere and array, after implementing the average approach for subject 552241. The resulting phosphene maps for the same subject when applying the individualized approach was shown in experiment 1, but are also shown in figure 16 for an easier comparison.

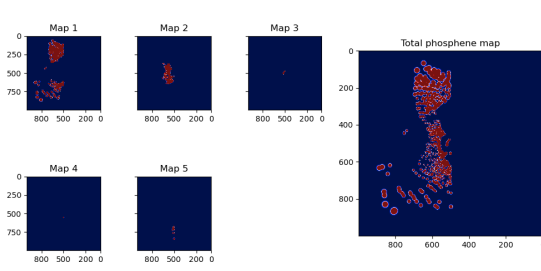


(a) Binarized phosphene map per array for the right hemisphere with the average approach.

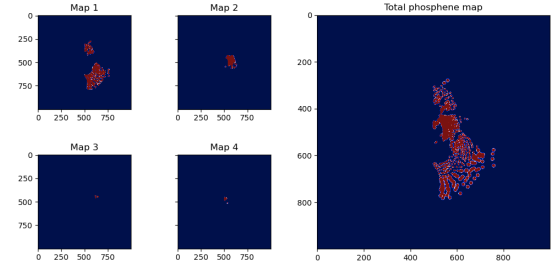


(b) Binarized phosphene map per array for the left hemisphere with the average approach.

Figure 15. Binarized phosphene maps per hemisphere and array using the average approach, for subject 552241.



(a) Binarized phosphene map per array for the right hemisphere with the individualized approach.



(b) Binarized phosphene map per array for the left hemisphere with the individualized approach.

Figure 16. Binarized phosphene maps per hemisphere and array using the individualized approach, for subject 552241.

Overall, not using the individualized approach resulted in the correct placement of substantially less arrays across subjects. Table 4 shows the total number of subjects, per approach and hemisphere, for which the procedure completed the placement of each array.

Array	Hemisphere	Subs completed with individualized	Subs completed with fsaverage
1	LH	181	181
2	LH	181	181
3	LH	181	158
4	LH	164	76
5	LH	116	19
1	RH	181	181
2	RH	181	165
3	RH	181	145
4	RH	170	87
5	RH	106	14

Table 4. Number of subjects with validly placed electrodes in both hemispheres per approach.

Figure 17 shows the mean cost function and its individual components per method and hemisphere based on the last successfully placed array. The yield loss was not meaningful for this visualization because it reflects the proportion of phosphene-evoking electrodes per array, while the violin plots are based on the last validly placed array with each method in each hemisphere. The figure shows that the mean cost is markedly lower for the individualized approach.

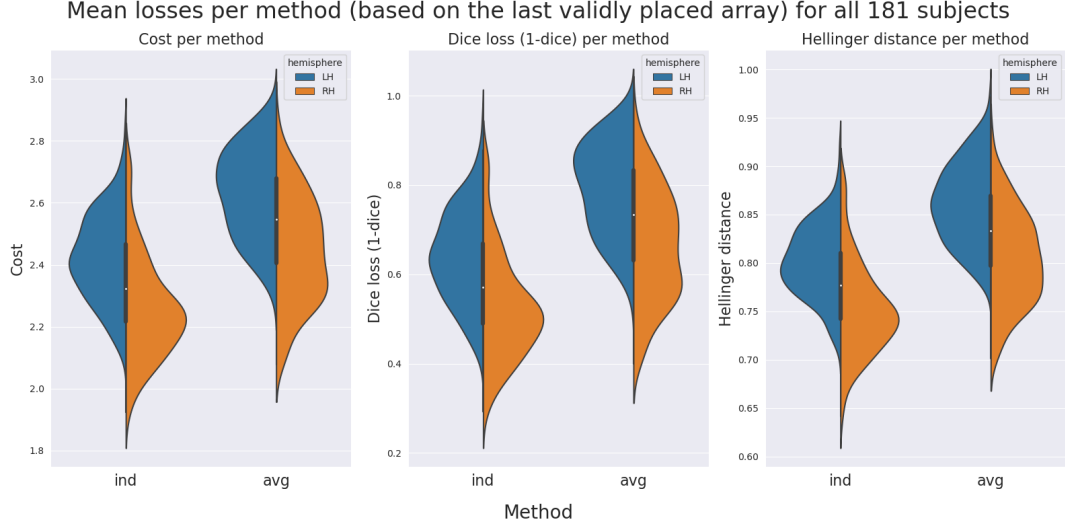


Figure 17. Mean losses per method and hemisphere for all 181 subjects, based on the last validly placed array.

The descriptive results per method and hemisphere are shown in the appendix section B.1, on table 10. To infer whether the individualized approach resulted in lower cost than the average approach, one paired samples t-test per hemisphere was conducted on the data of all 181 subjects, comparing the resulting cost function after successfully placing the last array. The results are shown in table 5. The necessary assumptions for the paired samples t-tests were met and are mentioned in the appendix section B.2.

Hemisphere	Factor	t value	DoF	p-value
LH	individual vs. average	-19.89	180	< 0.0001
RH	individual vs. average	-18.93	180	< 0.0001

Table 5. Results of paired samples t-test on the data of all subjects from each hemisphere.

Results showed that the individualized approach resulted in a statistically significant difference on the cost function compared to the average approach for both hemispheres. Specifically, for the left hemisphere the cost function for the individualized approach ($M = 2.42$, $SD = 0.14$) was significantly lower compared to the average ($M = 2.63$, $SD = 0.14$), $t(180) = -19.89$, $p < 0.0001$. Similarly, for the right hemisphere the individualized method ($M = 2.26$, $SD = 0.16$) performed significantly better than the average ($M = 2.44$, $SD = 0.17$), $t(180) = -18.93$, $p < 0.0001$.

4.2.3 Discussion

The aim of the second experiment was to explore whether the individualized approach, based on the individual anatomical scans, performed better than the average approach, where the optimization procedure was based on Freesurfer’s average brain. The results in section 4.2.2 show two important advantages of using the individualized approach. Firstly, the visual field coverage is substantially higher for the individualized approach, as is reflected through the lower cost function in figure 17. Secondly, and in relation to the first point, using the individualized approach, the optimization procedure completed the placement of substantially more arrays across all 181 subjects, as is shown on table 4. This suggests that the optimal location and array parameters found based on

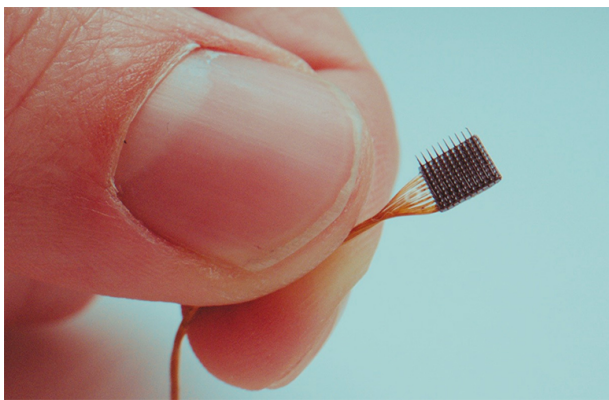
the average brain do not generalize well across individuals, especially as the number of arrays to be placed increases. For example, while the individualized approach successfully placed 4 arrays on 164 subjects for the left hemisphere, the average approach placed 4 arrays only on 76, a decrease of more than 50%. As such, using the individualized approach provides an important benefit on the visual field coverage.

This is a sensible result, since individuals don't have identical brain structures. While it is true that the location of the V1 brain area is highly predictable across individuals (Gazzaniga et al., 2019), there is still a lot of variation. Particularly, Benson et al. (2022) found that the size of visual areas V1, V2, and V3, varies dramatically across individuals, up to a factor of 3.5, which is much larger than the variability of the cerebral cortex size when considered as a whole. This variability explains why the optimization procedure based on the anatomical scans performs much better than the average approach.

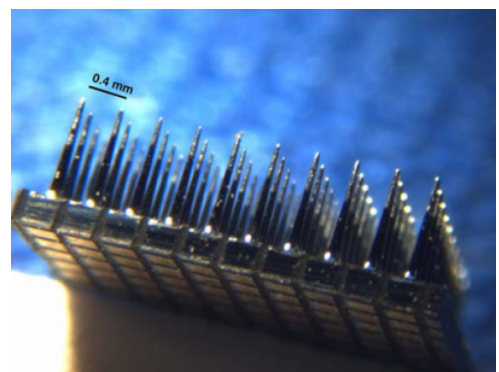
4.3 Experiment 3: Multiple Utah arrays vs multiple 3d arrays, based on individual scans

4.3.1 Experimental set-up and analysis

As mentioned in section 1.2, the array configuration used in experiments 1 and 2 is hypothetical and not currently available, thus making the results difficult to transfer to a research or clinical application. The third sub-question explores the implementation of an array configuration that is widely used both in research and practice, the Utah array (Blackrock-Neurotech, 2024), with a two-dimensional shape of $1 \times 10 \times 10$, giving a total of 100 electrodes. Since the array design and the electrode count on each array is much smaller, it is possible to implant a larger number of arrays. Based on previous research on implanting Utah arrays on monkeys (Chen et al., 2023, 2020), the procedure in experiment 3 is implemented for a total of 16 arrays. Similarly to the other experiments, the total number of arrays may end up to be smaller than 16, because it can be the case that the procedure did not find a valid placement for the last array(s) that yields a phosphene map. Importantly, the total number of electrodes with 16 such arrays is 1600, which is much less than the 5000 electrodes used in the hypothetical three-dimensional array. This of course has implications when comparing the phosphene maps of the two array designs, which are discussed in the results and discussion section.



(a) Utah array size. Image from Blackrock-Neurotech (2024)



(b) Utah array - distance between electrodes. Image from Kim et al. (2009, p. 2)

Figure 18. Illustration of a Utah array.

Since the goal of this experiment is to explore an implementation as close to the Utah

array as possible, the configuration was based on the array’s design as described in previous research (Kim et al., 2009) and the array’s manufacturer official website (Blackrock-Neurotech, 2024). An illustration of how the Utah array looks like is shown in figure 18, where 18a shows the Utah array with reference to a finger, while 18b shows a closer view of the Utah array specifying the distance between the electrodes, which is $0.4mm$. To keep the distance between the electrodes fixed at $0.4mm$ the *shank length* parameter had to be fixed as well. In the two-dimensional array simulation, the shank describes one row of 10 electrodes, so the length of the shank was fixed at $3.6mm$, thus not being included as a parameter to be optimized. Contrary to experiments 1 and 2, the optimization procedure for this set up ran for 100 iterations for each array. This was because the algorithm converged much quicker, since the array size is smaller and there is one less parameter to optimize. Additionally, to imitate a realistic implantation scenario, there was a minimum distance of $1.5mm$ between arrays for the placement to be considered valid. This reflects the length of the electrode shank, which according to (Blackrock-Neurotech, 2024), ranges between 1 and 1.5 mm. To re-iterate, the shank length of a real Utah array is 1 to 1.5 mm, and this is simulated by specifying the minimum distance between the arrays. For facilitating the simulation, the parameter *shank length* reflects one row of electrodes, and was fixed at $3.6mm$ to fix the distance between the electrodes at $0.4mm$. At the end of the optimization, the procedure returned the best optimization parameters for the placement of each array, for each hemisphere, and for each of the 181 subjects. The phosphene map generated by the last validly placed array after implementing the optimization with 16 Utah arrays is compared to the one after implementing the procedure with 5 three-dimensional arrays as described for experiment 1 in 4.1.

In a similar manner to the analysis in experiment 2, in 4.2.1, the results were analyzed per hemisphere, using a paired samples t-test, and using Bonferroni correction to adjust the significance level for multiple comparisons. In this case the independent variable is the array configuration, which has two levels: three-dimensional not (yet) existing array; and Utah array. All 181 subjects were compared on the basis of the last validly placed array, and the hypothesis was that the three-dimensional array configuration (which also optimizes the shank length) will result in a lower cost function compared to the two-dimensional Utah array (which has a fixed shank length). The statistics were performed using the Python library SciPy (Virtanen et al., 2020).

4.3.2 Results

This experiment compares the phosphene maps when applying the optimization procedure with different types of arrays. It is important to keep in mind that each Utah array has 100 electrodes, while each three-dimensional array has 1000 electrodes. As such, 16 Utah arrays result in 1600 electrodes, while 5 three-dimensional array result in 5000 electrodes, making the comparison relatively unequal. For this reason figure 19 shows how the cost function evolves for the different types of arrays as they keep increasing, allowing to compare the cost function for 10 Utah arrays and 1 three-dimensional array, with a total of 1000 electrodes. As discussed in the discussion part later in section 4.3.3, this comparison is still not equal because the phosphene map for the Utah array is underestimated, due to the small distance between the electrodes.

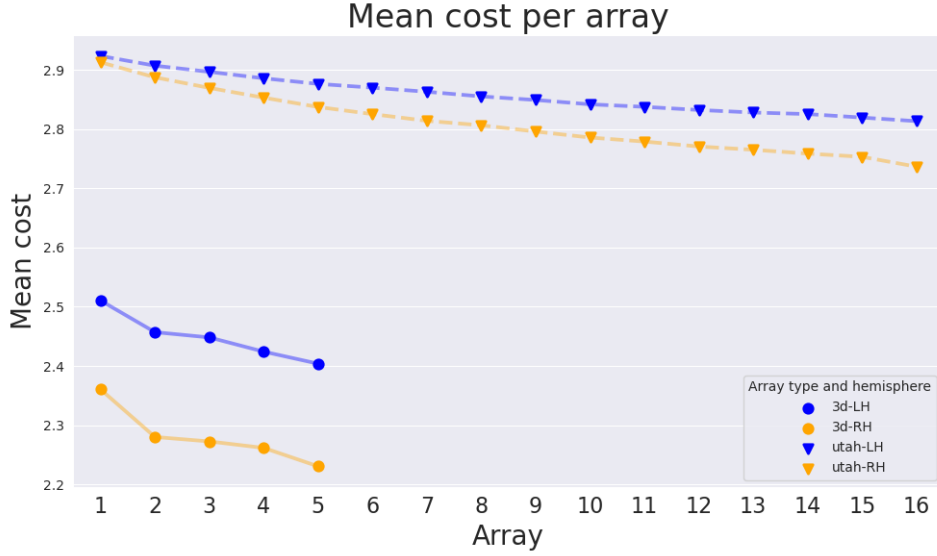


Figure 19. Mean cost per array type and hemisphere based on the number of subjects for which the procedure completed the placement of the corresponding array.

As explained in section 4.3.1, the distance between the electrodes for the Utah array is $0.4mm$ while for the three-dimensional arrays the distance between the electrodes on the shank can vary between $1.11mm$ and $2.22mm$, depending on the shank length. Given that the structural MRI scans have an isotropic voxel size of $0.7mm$, neighboring electrodes of a Utah array can fall within the same voxel. This limits the accuracy of the estimated phosphene map, since electrodes in the same voxel elicit identical phosphenes.

Figures 20 and 21 shows the resulting phosphene maps for the right hemisphere, while figures 22 and 23 for the left hemisphere, when using a simulation of the Utah array for subject 552241. For the same subject, the resulting phosphene maps when using the three-dimensional array are shown in the previous experiments, in figure 12.

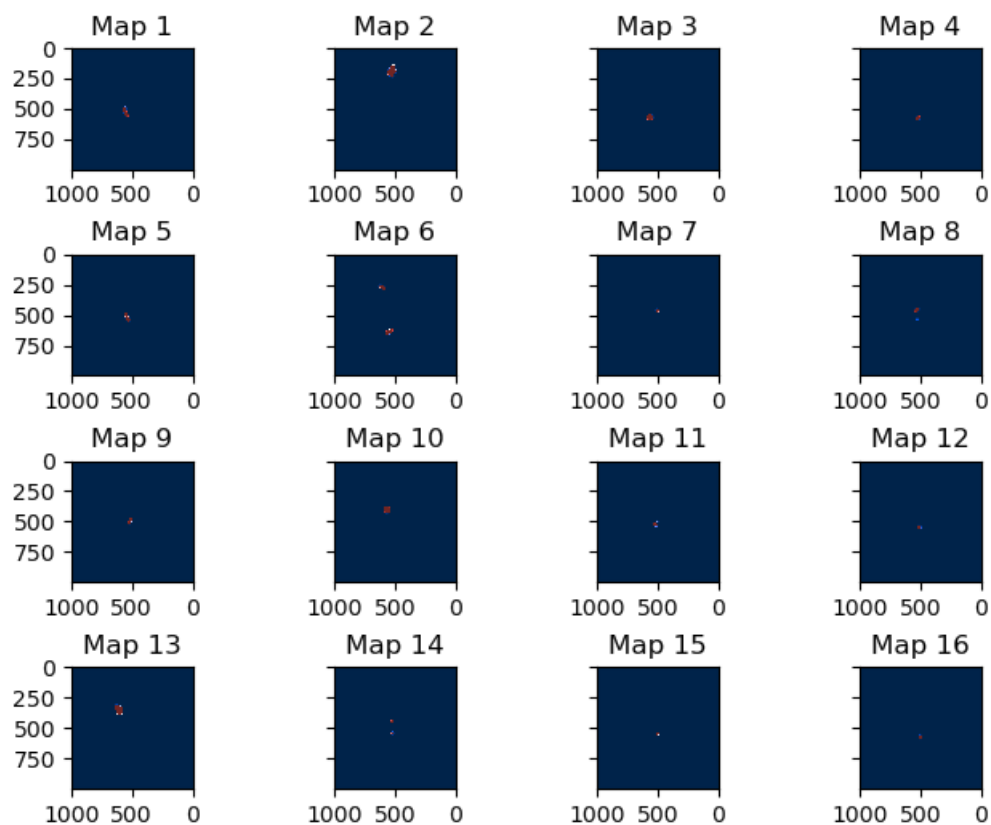


Figure 20. Binarized phosphene maps for each of the 16 Utah arrays for the right hemisphere, for subject 552241.

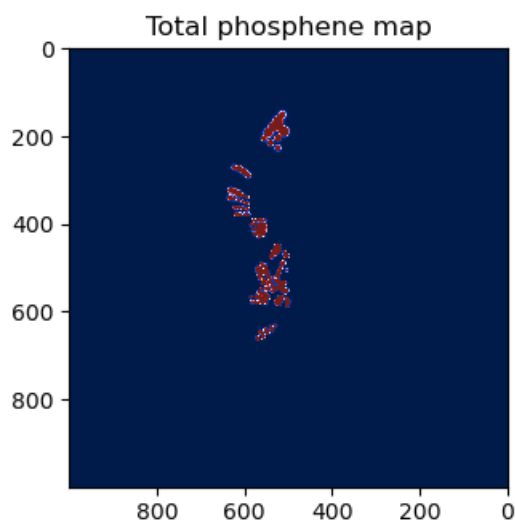


Figure 21. Total binarized phosphene map from all 16 Utah arrays for the right hemisphere, for subject 552241.

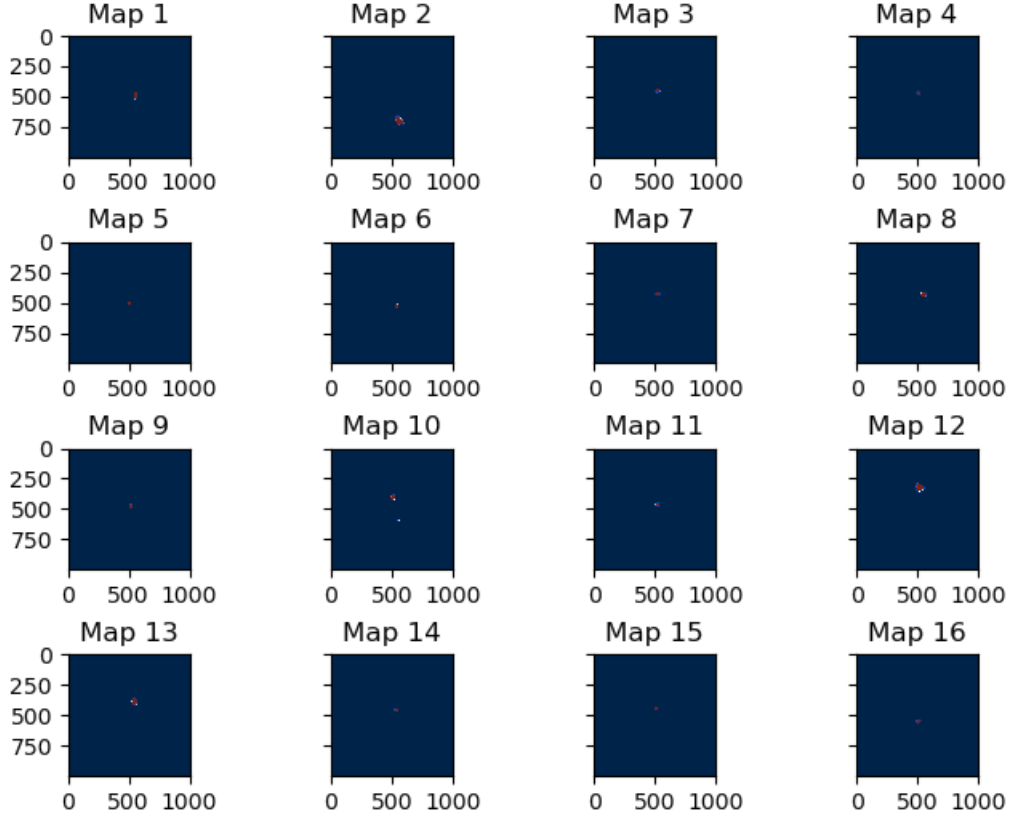


Figure 22. Binarized phosphene maps for each of the 16 Utah arrays for the left hemisphere, for subject 552241.

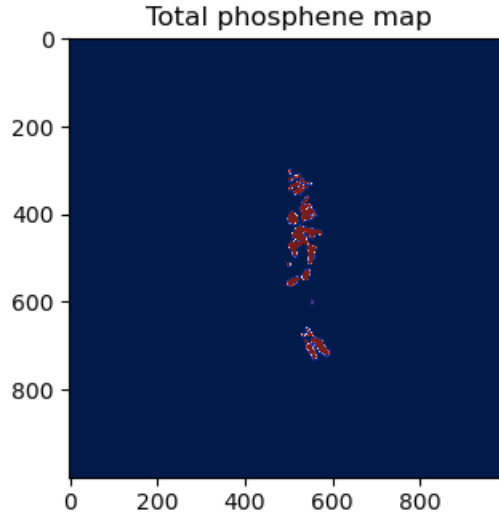


Figure 23. Total binarized phosphene map from all 16 Utah arrays for the left hemisphere, for subject 552241.

Figure 24 shows the mean cost function and its individual components for each type of array. Similarly to the reasoning for experiment 2 in B, the yield loss is not included, since it is based on each array individually, while here the visualization shows the metrics of the phosphene map resulting from the last validly placed array. The figure shows that the cost function for the three-dimensional array is substantially lower than that of the Utah array.

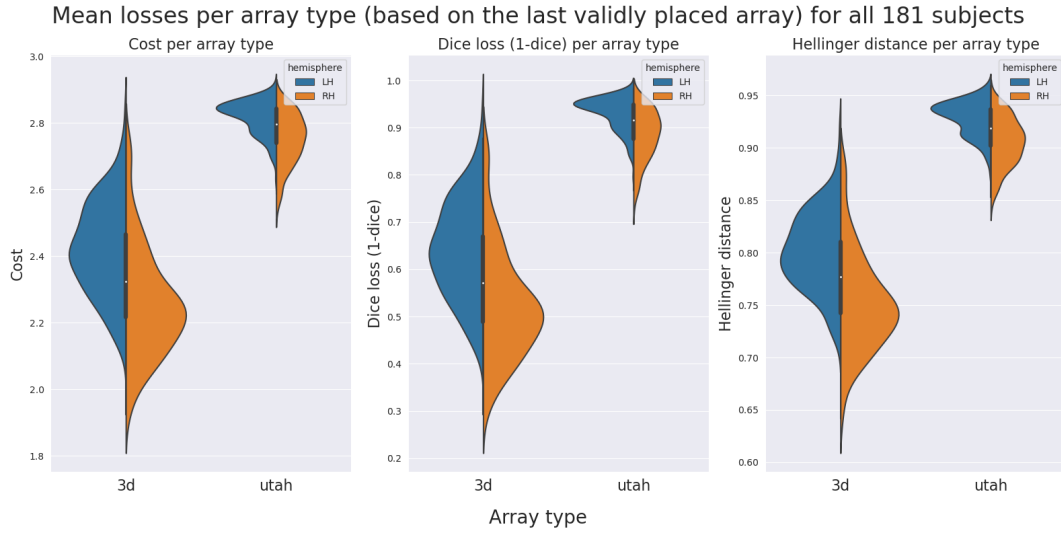


Figure 24. Mean losses per array type and hemisphere for all 181 subjects, based on the last validly placed array.

Figure 25 shows the mean yield loss per array type and hemisphere across all subjects for which the procedure completed the placement of the corresponding array. The yield loss is markedly lower for the Utah array compared to the three-dimensional array, meaning that the Utah array has a higher proportion of electrodes that fall in a voxel that yields a phosphene. However, because of the smaller distance between the electrodes of the Utah array, the estimated phosphenes is identical when the electrodes fall within the same voxel.

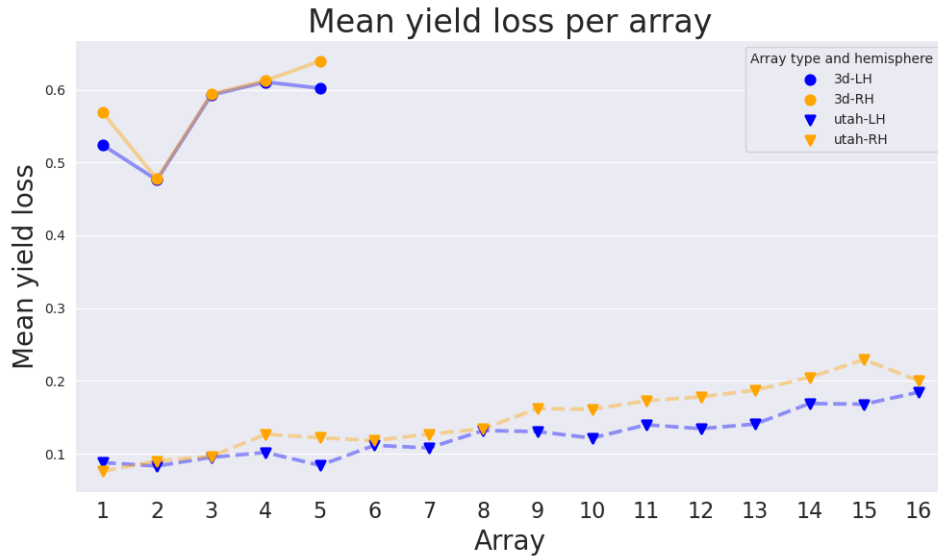


Figure 25. Mean yield loss per array type and hemisphere based on the number of subjects for which the procedure completed the placement of the corresponding array.

The descriptive results per array type and hemisphere are shown in the appendix section C.1, on table 11. To infer whether the three-dimensional array resulted in lower cost than the Utah array, one paired samples t-test per hemisphere was conducted on the data of all 181 subjects, comparing the resulting cost function after successfully placing

the last array. The results are shown in table 6. The necessary assumptions for the paired samples t-tests were met and are mentioned in the appendix section C.2.

Hemisphere	Factor	t value	DoF	p-value
LH	3d array vs. Utah	-43.96	180	< 0.0001
RH	3d array vs. Utah	-51.7	180	< 0.0001

Table 6. Results of paired samples t-test on the data of all subjects from each hemisphere.

Results showed that the three-dimensional array type resulted in a statistically significant difference on the cost function compared to the Utah array type for both hemispheres. It’s important to keep in mind that these results compare an unequal number of electrodes, namely 5000 for the three-dimensional array, and 1600 for the Utah array, and that the phosphene map for the Utah array is underestimated. With these considerations in mind, the cost function for the left hemisphere, for the three-dimensional array ($M = 2.42$, $SD = 0.14$) was significantly lower compared to the Utah array ($M = 2.82$, $SD = 0.05$), $t(180) = -43.96$, $p < 0.0001$. Similarly, for the right hemisphere the three-dimensional array ($M = 2.26$, $SD = 0.16$) performed significantly better than the Utah array ($M = 2.75$, $SD = 0.08$), $t(180) = -51.7$, $p < 0.0001$.

4.3.3 Discussion

The aim of the third experiment was to implement a currently available and broadly used array configuration, the Utah array, and explore whether the hypothetical three-dimensional array results in an improved visual field coverage compared to that of the Utah array. For this, the optimization procedure was performed for the placement of 16 two-dimensional Utah arrays of shape $1 \times 10 \times 10$, and was compared to the results of experiment 1, which used 5 arrays of shape $10 \times 10 \times 10$. As was expected, the results in section 4.2.2 show that the visual field coverage achieved by placing 5 three-dimensional arrays is substantially larger than that resulting from the placement of 16 Utah arrays, as is reflected through the lower cost values, shown in figure 24.

It is important to mention two critical considerations when examining the results from the placement of the Utah arrays. Firstly, the total number of electrodes that are placed are substantially less compared to that of the three-dimensional arrays. Particularly, 16 Utah arrays of the given shape result in a total of 1600 electrodes, while 5 three-dimensional arrays of the given shape contain 5000 electrodes. As such, it is sensible that the cost for the Utah arrays is higher. A more fair comparison would use the same number of electrodes between the different array designs, for example by comparing 10 Utah arrays to 1 three-dimensional array.

However, as can be seen from comparing the example phosphene maps for 10 Utah arrays in figure 22 to the phosphene map for 1 three-dimensional array in figure 12, the visual field coverage is substantially larger for the three-dimensional array. This is also reflected in figure 19, which visualized the respective cost functions. This highlights the second consideration when implementing the Utah arrays, which has to do with the estimation of the phosphene map. As was mentioned in section 3.2.1, the retinotopy data have an isotropic resolution of $1mm$ (Benson et al., 2018), while the distance between the electrodes for the Utah arrays is $0.4mm$, and for the three-dimensional arrays this distance ranges between $1.1mm$ and $2.2mm$, depending on the length of the electrode shank, while the distance between the shanks is fixed at $1mm$. This means that for Utah arrays, two or three electrodes could fall within the same voxel thus resulting in identical

predicted phosphenes. At the same time this cannot happen for the three-dimensional array because of the larger distance between the electrodes, so the spatial coverage of the Utah array is underestimated compared to that of the three-dimensional array.

A solution for this would require a retinotopy dataset of higher resolution, with an isotropic voxel of less than $0.4mm$. This is not an unrealistic scenario, since Lüsebrink, Sciarra, Mattern, Yakupov, and Speck (2017) have developed a technology for acquiring structural scans for T1-weighted images with an isotropic resolution between $0.25mm$ and $0.35mm$. Even though the task of acquiring such a retinotopy dataset with such an increased resolution is greatly ambitious, it could pave the way for significantly more accurate simulations that could be more informative when it comes to the implementation of current array designs, like the Utah array.

Alternatively, since the retinotopy data have clear gradients (Benson et al., 2018), one could upsample and interpolate to estimate the phosphene map when using such a small distance between the electrodes, like $0.4mm$. However, this would create a high resolution prediction for the phosphene map, which is not necessarily accurate. Another option would be to downsample the target map, or create target maps that are convolved with the receptive fields of all voxels in a given area, as the map shown in figure 10b. Nonetheless, since the the three-dimensional array configuration allows a wider electrode spacing than the Utah array, the spatial coverage will likely be better, even with an equal number of electrodes.

5 General discussion

The main aim of this research was to develop a Bayesian optimization algorithm for the efficient placement of multiple electrode arrays of different designs in the V1 brain area, for visual cortical prostheses. This section presents a discussion of how the findings relate to relevant previous research 5.1, the societal and clinical implications of this research 5.2, as well as its limitations and suggestions for future research 5.3.

5.1 Relation to theory and previous research

The current research extends the work by van Hoof et al. (2024) to effectively optimize the placement of several arrays in the V1 brain area. Additionally, it implements the optimization procedure for a type of array that is widely used in research and clinical practice, the Utah array. The results are in line both with the findings by van Hoof et al. (2024), and also with what is known about retinotopic mapping. Particularly, it was expected that including a higher count of electrodes would result in a higher visual field coverage, and that the individualized approach would yield better results than the average approach.

An issue that still remains to be explored from a theoretical perspective, is how phosphenes that are elicited from stimulating different brain areas are perceptually combined into patterns. This is relevant for research on phosphene simulation because it provides a deep insight into how the perceptual information by the stimulation of different visual areas would be combined. Currently, the algorithm in this research can be easily configured to optimize the array placement based on multiple brain areas. For example, it can be configured to optimize the foveal representation for the V1 area, while optimizing the more peripheral part of the visual field for later visual areas. However, there is still room for research into how the predicted phosphenes perceptually add up, and what visual features can be conveyed in this way. In normal vision, the brain integrates the neural signals from the visual areas into a unified visual percept, where each visual area captures different aspects of the visual stimulus (Kandel et al., 2014). For example, V1 conveys information about orientation or edges, while higher-order visual areas convey information about texture or motion (Kandel et al., 2014). Elucidating the way the phosphenes that are generated from distinct visual areas are perceptually combined into patterns would allow for more possible configurations for a visual prosthesis.

Another issue that remains to be explored from a theoretical perspective, is how white matter stimulation may influence perception. White matter refers to the myelinated axons of neurons, ie. the part that transfers information among neurons, while grey matter refers to the cell body of the neuron (Gazzaniga et al., 2019). Currently, although white matter within visual areas carries visual information, there is no clear information for a retinotopic mapping of white matter (van Hoof et al., 2024), so the predicted phosphene map was estimated by stimulating electrodes placed only within grey matter. However, a large part of the electrode arrays was likely located within white matter, so elucidating the role of white matter stimulation is important for more accurate phosphene prediction.

Lastly, the distance between the electrode arrays seems to play an important role in the stability of the prosthesis and on the health of the neural tissue (Chen et al., 2023). Specifically, placing the arrays closer together may have a negative impact on the tissue, so it is important to take that into account when planning the placement of multiple arrays. The optimization procedure allows to specify the desired minimum

distance in millimeters by only changing one value in the configuration file, so it can be easily adjustable to different surgical needs.

5.2 Societal relevance and clinical implications

Establishing a technology that can restore a rudimentary form of vision in people with blindness is undoubtedly a remarkable feat that can greatly enhance the quality of life for a lot of people. Currently, it is estimated that around 43 million people live with complete blindness (Orbis international, 2021), and so far there has been no established way that can help them experience again a visual form of the environment. Therefore, research on advanced visual prostheses that can help them perceive a rudimentary form of the environment bears high societal relevance, and recent efforts have made the first steps onto implementing such a prosthesis in a human subject (Fernández et al., 2021).

Establishing such an advanced visual prosthesis is a highly ambitious aim that involves several components. It is also an inherently interdisciplinary effort, spanning across several scientific disciplines, from neural and electrical engineering, neuroscience, and artificial intelligence (van der Grinten et al., 2024). The current simulation research contributed to the challenges of finding the optimal placement and array parameters for maximizing the similarity between the target and the predicted phosphene maps.

The findings are highly relevant for future clinical and research applications, as they are informative both about the array design, as well as the location parameters in the brain. Particularly, the so-far-hypothetical three-dimensional array seems to be highly beneficial in terms of visual field coverage, so it would be meaningful for array design researchers to manufacture such a multi-electrode probe. Additionally, since the current procedure also allows to easily simulate new array designs, it could be used to test novel array configurations and explore more possibilities for a new array design.

The current simulation procedure also finds the optimal placement location within the V1 brain area, and can easily be configured for placement in other visual areas as well, while specifying the target visual field coverage and resolution. As such, given the patient’s anatomical scans, clinical and research application could use this procedure according to the patient’s needs or the goals of the research, so that the eventual stimulation-evoked phosphenes match the predetermined target. The procedure also considers practical boundaries, like whether the array falls outside of the grey matter area and the minimum allowed distance between the electrode arrays. It is also flexible, so that it can be easily adjusted to other constraints that may emerge.

5.3 Limitations and future research

To understand the limitations of this research, it is useful to reiterate some important elements of the procedure. The predicted phosphene map that is generated by stimulating the implanted electrodes is unknown, and is estimated from the underlying population receptive field maps, as derived from the anatomical scans. Therefore, the spatial resolution and the precision of the phosphene map depends on the pRF maps and the resolution of the MRI scans. As was mentioned in section 4.3.3, when the distance between the electrodes on the array is smaller than the isotropic voxel resolution of the retinotopy dataset, some electrodes fall within the same voxel. This results in identical predicted phosphenes for these electrodes, thus providing an underestimation of the predicted phosphene map.

Another consideration for this research, is that although it accounts for the practical constraints of grey matter and the overlapping arrays, it does not account for the arterial architecture of the brain (van Hoof et al., 2024). The brain’s vasculature is essential for providing nutrients that are necessary for the proper functioning of the central nervous system (Konan, Reddy, & Mesfin, 2023), so it would be undesirable to harm its functioning. Anatomical and angiographic studies provide a lot of detail on the topography of the arterial architecture, so the current pipeline could be extended to avoid crossing tissue that is critical for blood supply to the brain.

Lastly, an additional consideration is the serial approach with which the array location and parameters are being optimized. The procedure finds the optimal parameters iteratively for each array, and as a result, the optimal parameters for the first array may end up to be sub-optimal when considering the placement of additional arrays. Future research could develop more intricate optimization procedures, for example by allowing the re-evaluation of previously placed arrays based on the next one.

6 Conclusion

The current research has provided a Bayesian optimization pipeline for the informed placement of multi-array brain electrodes for advanced visual cortical prostheses. Results showed that the inclusion of additional arrays provides a substantial increase in visual field coverage, and that using individual anatomical scans outperforms average brain solutions. The procedure finds the array parameters and electrode placement location in the brain that provides the closest match to a predetermined visual field coverage. In addition, it can be easily configured to simulate different array designs, vary the target visual field coverage, include an arbitrary number of arrays per hemisphere, as well as incorporate additional constraints by modifying the cost function. It also provides a simulated implementation of the Utah array, which is widely used in research and clinical practice, thus aiming to provide a useful tool in pre-operative surgical procedures using the Utah array. This has important societal implications, since establishing advanced visual cortical prostheses that restore a rudimentary form of vision would enhance the quality of life of blind patients.

References

- Agresti, A., & Franklin, C. (2009). *Statistics: The art and science of learning from data*. Pearson Education.
- Beauchamp, M., Oswalt, D., Sun, P., Foster, B., Magnotti, J., Niketeghad, S., . . . Yoshor, D. (2020). Dynamic stimulation of visual cortex produces form vision in sighted and blind humans. *Cell*, *181*, 774-783. doi: 10.1016/j.cell.2020.04.033
- Benson, N. C., Butt, O., Brainard, D., & Aguirre, G. (2014). Correction of distortion in flattened representations of the cortical surface allows prediction of v1-v3 functional organization from anatomy. *PLoS computational biology*, *10*. doi: 10.1371/journal.pcbi.1003538
- Benson, N. C., Butt, O., Datta, R., Radoeva, P., Brainard, D., & Aguirre, G. (2012). The retinotopic organization of striate cortex is well predicted by surface topology. *Current biology*, *22*. doi: 10.1016/j.cub.2012.09.014
- Benson, N. C., Jamison, K. W., Arcaro, M. J., Vu, A. T., Glasser, M. F., Coalson, T. S., . . . Kay, K. (2018). The human connectome project 7 tesla retinotopy dataset: Description and population receptive field analysis. *Journal of Vision*, *18*(13), 23-23. Retrieved from <https://doi.org/10.1167/18.13.23> doi: 10.1167/18.13.23
- Benson, N. C., Kupers, E. R., Barbot, A., Carrasco, M., & Winawer, J. (2021, August). Cortical magnification in human visual cortex parallels task performance around the visual field. *eLife*, *10*, e67685. Retrieved from <https://doi.org/10.7554/eLife.67685> doi: 10.7554/eLife.67685
- Benson, N. C., Yoon, J. M. D., Forenzo, D., Engel, S. A., Kay, K. N., & Winawer, J. (2022). Variability of the surface area of the v1, v2, and v3 maps in a large sample of human observers. *Journal of Neuroscience*, *42*(46), 8629-8646. Retrieved from <https://www.jneurosci.org/content/42/46/8629> doi: 10.1523/JNEUROSCI.0690-21.2022
- Black, P. E. (2022, February). Greed algorithm. In P. E. Black (Ed.), *Dictionary of algorithms and data structures*. Retrieved from <https://www.nist.gov/dads/HTML/greedyalgo.html>
- Blackrock-Neurotech. (2024). *Utah neuroport array*. Retrieved 2024-02-24, from <https://blackrockneurotech.com/products/neuroport-array/>
- Brindley, G. S., & Lewin, W. S. (1968). The sensations produced by electrical stimulation of the visual cortex. *The Journal of Physiology*, *194*(2).
- Brochu, E., Cora, V., & Freitas, N. (2010). A tutorial on bayesian optimization of expensive cost functions, with application to active user modeling and hierarchical reinforcement learning. *Computing Research Repository*, *abs/1012.2599*. Retrieved from <http://arxiv.org/abs/1012.2599>
- Chen, X., Wang, F., Fernandez, E., & Roelfsema, P. (2020). Shape perception via a high-channel-count neuroprosthesis in monkey visual cortex. *Science*, *370*, 1191-1196. doi: 10.1126/science.abd7435
- Chen, X., Wang, F., Kooijmans, R., Klink, P. C., Boehler, C., Asplund, M., & Roelfsema, P. R. (2023, June). Chronic stability of a neuroprosthesis comprising multiple adjacent utah arrays in monkeys. *Journal of Neural Engineering*, *20*(3), 36-39. Retrieved from <https://dx.doi.org/10.1088/1741-2552/ace07e> doi: 10.1088/1741-2552/ace07e
- Curing retinal blindness foundation. (2023). *Tools of the blind and visually impaired*. Retrieved 2023-09-14, from <https://www.crb1.org/for-families/resources/>

- tools/
- Dawson-Haggerty et al. (2024). *trimesh*. Retrieved from <https://trimesh.org/>
- de Ruyter van Steveninck, J., van Gestel, T., Koenders, P., van der Ham, G., Vereecken, F., Güçlü, U., ... van Wezel, R. (2022, February 1). Real-world indoor mobility with simulated prosthetic vision: The benefits and feasibility of contour-based scene simplification at different phosphene resolutions. *Journal of Vision*, 22(2), 1. doi: 10.1167/jov.22.2.1
- Dobelle, W. H., Mladejovsky, M. G., & Girvin, J. P. (1974). Artificial vision for the blind: Electrical stimulation of visual cortex offers hope for a functional prosthesis. *Science*, 183, 440-444. doi: 10.1126/science.183.4123.440
- Fernández, E., Alfaro, A., Soto-Sánchez, C., Gonzalez-Lopez, P., Lozano, A. M., Peña, S., ... Normann, R. A. (2021). Visual percepts evoked with an intracortical 96-channel microelectrode array inserted in human occipital cortex. *The Journal of Clinical Investigation*, 131(23). Retrieved from <https://www.jci.org/articles/view/151331> doi: 10.1172/JCI151331
- Frazier, P. I. (2018). A tutorial on bayesian optimization. *arXiv*. Retrieved from <https://arxiv.org/pdf/1807.02811.pdf> doi: 10.48550/arXiv.1807.02811
- Gazzaniga, M., Ivry, R. B., & Mangun, G. R. (2019). *Cognitive neuroscience: The biology of the mind* (5th ed.). W. W. Norton & Company.
- Greenwood, M. (2022). *Multiple (pair-wise) comparisons using tukey's hsd and the compact letter display*. Retrieved 2024-04-07, from [https://stats.libretexts.org/Bookshelves/Advanced_Statistics/Intermediate_Statistics_with_R_\(Greenwood\)/03%3A_One-Way_ANOVA/3.06%3A_Multiple_\(pair-wise\)_comparisons_using_Tukeys_HSD_and_the_compact_letter_display](https://stats.libretexts.org/Bookshelves/Advanced_Statistics/Intermediate_Statistics_with_R_(Greenwood)/03%3A_One-Way_ANOVA/3.06%3A_Multiple_(pair-wise)_comparisons_using_Tukeys_HSD_and_the_compact_letter_display)
- Heitmann, C., Zhan, M., Linke, M., Hölig, C., Kekunnaya, R., van Hoof, R., ... Röder, B. (2023, November 20). Early visual experience refines the retinotopic organization within and across visual cortical regions. *Current Biology*, 33(22), 4950–4959.e4. doi: 10.1016/j.cub.2023.10.010
- Himmelberg, M. M., Winawer, J., & Carrasco, M. (2023). Polar angle asymmetries in visual perception and neural architecture. *Trends in Neurosciences*, 46(6), 445-458. Retrieved from <https://www.sciencedirect.com/science/article/pii/S0166223623000681> doi: 10.1016/j.tins.2023.03.006
- INTENSE: Innovative Neurotechnology for Society. (2023). *Home page*. Retrieved 2024-03-14, from <https://intenseproject.eu/>
- Kandel, E. R., Schwartz, J. H., Jessell, T. M., Siegelbaum, S. A., Hudspeth, A. J., & Mack, S. (2014). *Principles of neural science* (Fifth ed.). McGraw-Hill Education. Retrieved from <https://neurology.mhmedical.com/content.aspx?bookid=1049§ionid=59138139>
- Kim, S., Bhandari, R., Klein, M., Negi, S., Rieth, L., Tathireddy, P., ... Solzbacher, F. (2009). Integrated wireless neural interface based on the utah electrode array. *Biomedical Microdevices*, 11(2), 453-466. Retrieved from <https://eurekamag.com/research/053/893/053893033.php> doi: 10.1007/s10544-008-9251-y
- Konan, L., Reddy, V., & Mesfin, F. (2023). Neuroanatomy, cerebral blood supply. *StatPearls*. Retrieved from <https://www.ncbi.nlm.nih.gov/books/NBK532297/>
- Limburg, H., & Keunen, J. E. E. (2009). Blindness and low vision in the netherlands from 2000 to 2020-modeling as a tool for focused intervention. *Ophthalmic Epidemiology*, 16, 362–369. doi: 10.3109/09286580903312251
- Lizotte, D. J. (2008). *Practical bayesian optimization* (Unpublished doctoral dissertation).

- University of Alberta.
- Lüsebrink, F., Sciarra, A., Mattern, H., Yakupov, R., & Speck, O. (2017, 03). T1-weighted in vivo human whole brain mri dataset with an ultrahigh isotropic resolution of 250 μm . *Scientific Data*, 4, 170032. doi: 10.1038/sdata.2017.32
- Muhammad, L. (2023, 06). Guidelines for repeated measures statistical analysis approaches with basic science research considerations. *Journal of Clinical Investigation*, 133. doi: 10.1172/JCI171058
- Neuronexus. (2024). *Electrode arrays: 3d probes*. Retrieved 2024-02-24, from <https://www.neuronexus.com/products/electrode-arrays/3dprobes/>
- Niketeghad, S., & Pouratian, N. (2018). Brain machine interfaces for vision restoration: The current state of cortical visual prosthetics. *Neurotherapeutics*, 16, 134-143. doi: 10.1007/s13311-018-0660-1
- Orbis international. (2021). *Global blindness was slowing prior to pandemic study reveals*. Retrieved 2023-09-14, from <https://www.orbis.org/en/news/2021/new-global-blindness-data>
- Quadrianto, N., Kersting, K., & Xu, Z. (2010). Gaussian process. In C. Sammut & G. I. Webb (Eds.), *Encyclopedia of machine learning* (pp. 428-439). Boston, MA: Springer US. Retrieved from https://doi.org/10.1007/978-0-387-30164-8_324 doi: 10.1007/978-0-387-30164-8_324
- Rasmussen, C. E., & Williams, C. K. I. (2005). *Gaussian processes for machine learning*. The MIT Press. Retrieved from <https://doi.org/10.7551/mitpress/3206.001.0001> doi: 10.7551/mitpress/3206.001.0001
- Ray team. (2024). *Ray*. Retrieved from <https://docs.ray.io/en/latest/ray-more-lib/multiprocessing.html>
- Rios, G., Lubenov, E. V., Chi, D., Roukes, M. L., & Siapas, A. G. (2016). Nanofabricated neural probes for dense 3-d recordings of brain activity. *Nano letters*, 16(11), 6857-6862.
- Roelfsema, P. R. (2020). Writing to the mind's eye of the blind. *Cell*, 181, 758-759. doi: 10.1016/j.cell.2020.03.014
- scikit-optimize. (2024). *scikit-optimize*. Retrieved 2024-03-13, from <https://scikit-optimize.github.io/stable/>
- Seabold, S., & Perktold, J. (2010). statsmodels: Econometric and statistical modeling with python. In *9th python in science conference*.
- Shi, Y. (2019). Gaussian processes, not quite for dummies. *The Gradient*. <https://thegradient.pub/machine-learning-ancient-japan/>.
- Tehovnik, E. J., Slocum, W. M., Carvey, C. E., & Schiller, P. H. (2005). Phosphene induction and the generation of saccadic eye movements by striate cortex. *Journal of Neurophysiology*, 93(1), 1-19. Retrieved from <https://doi.org/10.1152/jn.00736.2004> doi: 10.1152/jn.00736.2004
- Tootell, R. B. H., Switkes, E., Silverman, M. S., & Hamilton, S. L. (1988). Functional anatomy of macaque striate cortex. ii. retinotopic organization. *Journal of Neuroscience*, 8(5), 1531-1568. Retrieved from <https://www.jneurosci.org/content/8/5/1531> doi: 10.1523/JNEUROSCI.08-05-01531.1988
- Vallat, R. (2018, November). Pingouin: Statistics in python. *The Journal of Open Source Software*, 3(31), 1026.
- van der Grinten, M., de Ruyter van Steveninck, J., Lozano, A., Pijnacker, L., Rueckauer, B., Roelfsema, P., ... Güçlütürk, Y. (2024, February 22). Towards biologically plausible phosphene simulation for the differentiable optimization of visual cortical

- prostheses. *eLife*, 13, 1–25. doi: 10.7554/eLife.85812
- van Hoof, R. (2022). *The brain as image processor and generator: Towards function-restoring brain-computer-interfaces* (Doctoral dissertation, Maastricht University). doi: 10.26481/dis.20220603rh
- van Hoof, R., Lozano, A., Wang, F., Klink, P. C., Roelfsema, P. R., & Goebel, R. (2024). Optimal placement of high-channel visual prostheses in human retinotopic visual cortex. *bioRxiv*. Retrieved from <https://www.biorxiv.org/content/early/2024/03/11/2024.03.05.583489> doi: 10.1101/2024.03.05.583489
- Van Rossum, G., & Drake, F. L. (2009). *Python 3 reference manual*. Scotts Valley, CA: CreateSpace.
- Virtanen, P., Gommers, R., Oliphant, T. E., Haberland, M., Reddy, T., Cournapeau, D., ... SciPy 1.0 Contributors (2020). SciPy 1.0: Fundamental algorithms for scientific computing in Python. *Nature Methods*, 17, 261–272. doi: 10.1038/s41592-019-0686-2
- Zardini, A. S., Rostami, B., Najafi, K., Hetrick, V. L., & Ahmed, O. J. (2021). Sea of electrodes array (sea): Extremely dense and high-count silicon-based electrode array technology for high-resolution high-bandwidth interfacing with 3d neural structures. *bioRxiv*. Retrieved from <https://www.biorxiv.org/content/early/2021/01/26/2021.01.24.427975> doi: 10.1101/2021.01.24.427975

A Experiment 1 results

A.1 Descriptive results

Array	Hem.	Subs completed	Dice loss	Prop. dice	Yield loss	HD	Prop. HD	Cost	Prop. cost
1	LH	181	0.71	0.39	0.52	0.83	0.56	2.51	0.31
2	LH	181	0.67	0.44	0.48	0.81	0.61	2.46	0.35
3	LH	181	0.66	0.46	0.59	0.81	0.62	2.45	0.35
4	LH	164	0.64	0.48	0.61	0.8	0.64	2.42	0.37
5	LH	116	0.63	0.5	0.6	0.8	0.65	2.4	0.38
1	RH	181	0.6	0.5	0.57	0.78	0.6	2.36	0.41
2	RH	181	0.55	0.56	0.48	0.76	0.66	2.28	0.46
3	RH	181	0.54	0.57	0.59	0.76	0.67	2.27	0.47
4	RH	170	0.53	0.58	0.61	0.75	0.67	2.26	0.47
5	RH	106	0.5	0.6	0.64	0.74	0.69	2.23	0.49

Table 7. Results table with average losses per hemisphere and array.

Table 7 shows all mean metrics per hemisphere for each array. The linearly weighted cost function, as well as its individual components, dice loss and Hellinger distance, are computed by comparing the generated phosphene map to the full target map shown in figure 10a. However, as was mentioned in section 3.2.4, such a phosphene map cannot be generated by stimulating only neurons in the V1 brain area. As such, table 7 also shows the loss components in proportion to the scenario of stimulating all neurons in V1. For example, if the dice loss is 0.63, and hence the dice is 0.37 after implanting the fifth array, the proportion of this dice to the best possible phosphene map that can be generated by stimulating all neurons in V1 is 0.5. So it covers 50% of the best possible dice that can be achieved by stimulating all neurons in V1. The same has been calculated for phosphene density, as is reflected in the Hellinger distance metric.

A.2 Assumptions for repeated measures ANOVA

For repeated measures ANOVA to provide an appropriate statistical inference, several assumption need to be met. Specifically, the categorical independent variable needs to have at least three levels; the continuous dependent variable needs to be approximately normally distributed and without outliers for each level of the independent variables; there is homogeneity of variance of the dependent variable across all levels of the independent variables, also referred to as *homoscedasticity*; and the variance of the differences between all possible pairs of the levels of the independent variables are equal, also referred to as *sphericity* (Muhammad, 2023). Since the statistics to validate the assumptions were run twice, once for each hemisphere, the standard significance level for the p-value, 0.05, was divided by 2, so it was set to 0.025.

Figure 26 shows that the distributions of the cost function per hemisphere, for each array, ie. each level of the independent variable, approximate a normal distribution. Even if the cost function deviates from a normal distribution for some of the arrays, this does not pose an issue for a repeated measures ANOVA. This is because according to the Central Limit Theorem, the sampling distribution of the means tends to approximate a normal distribution regardless of the distribution of the data, as long as the sample size is sufficiently large, typically larger than 30 (Agresti & Franklin, 2009).

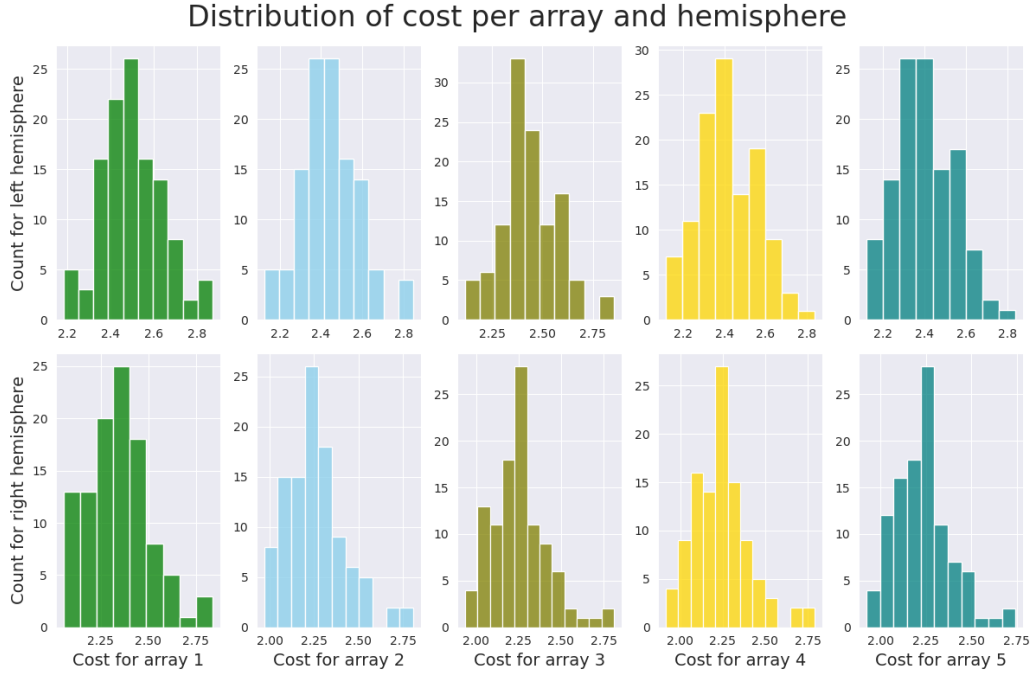


Figure 26. Histograms of the cost function for each array per hemisphere.

Table 8 presents the relevant statistical tests for the assumptions of homoscedasticity and sphericity for each hemisphere, as were calculated using the Python library pingouin (Vallat, 2018). These statistics test against the null hypothesis that the assumption is met, so if the p-value is greater than 0.025, the null cannot be rejected and the assumption is met. Specifically, Mauchly’s test of sphericity showed that the assumption is met both for the left ($\chi^2 = -1500.8$, $p = 1$) and for the right ($\chi^2 = -1503.84$, $p = 1$) hemisphere. Similarly, Levene’s test of homoscedasticity showed that the assumption is met for the left ($W = 0.1$, $p = 0.98$) and the right ($W = 0.12$, $p = 0.97$) hemisphere as well.

Hemisphere	Assumption	Statistical test	Statistic	p-value	Assumption met
LH	sphericity	Mauchly’s	$\chi^2 = -1500.8$	1	True
LH	homoscedasticity	Levene’s	$W = 0.1$	0.98	True
RH	sphericity	Mauchly’s	$\chi^2 = -1503.84$	1	True
RH	homoscedasticity	Levene’s	$W = 0.12$	0.97	True

Table 8. Statistics for the assumptions of repeated measures ANOVA.

A.3 Post-hoc pairwise comparisons with Tukey’s HSD test

Hemisphere	Array pair	Mean difference	Std difference	p-value adj.	Significant
LH	1-2	0.0596	0.037	0.0117	True
LH	1-3	0.0696	0.0551	0.0017	True
LH	1-4	0.0892	0.0835	< 0.0001	True
LH	1-5	0.1001	0.0851	< 0.0001	True
LH	2-3	0.01	0.035	0.9831	False
LH	2-4	0.0296	0.0786	0.498	False
LH	2-5	0.0405	0.0806	0.1847	False
LH	3-4	0.0196	0.0743	0.827	False
LH	3-5	0.0305	0.0783	0.4658	False
LH	4-5	0.0109	0.0293	0.9765	False
RH	1-2	0.0846	0.047	0.0017	True
RH	1-3	0.092	0.0641	0.0005	True
RH	1-4	0.1034	0.0707	0.0001	True
RH	1-5	0.1138	0.0777	< 0.0001	True
RH	2-3	0.0074	0.0249	0.9975	False
RH	2-4	0.0188	0.0401	0.9197	False
RH	2-5	0.0292	0.056	0.6921	False
RH	3-4	0.0114	0.0318	0.9868	False
RH	3-5	0.0218	0.0515	0.8687	False
RH	4-5	0.0104	0.0408	0.9905	False

Table 9. Post-hoc pairwise comparisons using Tukey’s HSD test.

The table shows all pairwise comparisons for the subjects that completed the placement of 5 arrays per hemisphere. These are 116 for the left hemisphere and 106 for the right.

B Experiment 2 results

B.1 Descriptive results

Method	Hem.	Max array	Dice loss	Prop. dice	Yield loss	HD	Prop. HD	Cost	Prop. cost
ind	LH	4.55	0.64	0.48	0.61	0.8	0.64	2.42	0.37
avg	LH	3.4	0.79	0.28	0.57	0.86	0.45	2.63	0.23
ind	RH	4.52	0.52	0.59	0.63	0.75	0.68	2.26	0.48
avg	RH	3.27	0.66	0.42	0.57	0.8	0.54	2.44	0.36

Table 10. Results table with average losses per method and hemisphere for all 181 subjects.

Table 10 shows all mean metrics per hemisphere for each method. As described for the results of experiment 1 in the appendix A.1, the proportional columns refer to the proportion that each metric covers relative to the scenario of stimulating all phosphene evoking neurons in V1.

B.2 Assumptions for paired samples t-test

As with repeated measures ANOVA described in the appendix above A.2, for the paired samples t-test to yield a valid inference, several assumption need to be met. Specifically, the categorical independent variable needs to have two levels; the continuous de-

pendent variable needs to be approximately normally distributed and without outliers for each level of the independent variable; and the observations should be independent.

Figure 27 shows that the distributions of the cost function per hemisphere, for each method, ie. each level of the independent variable, approximate a normal distribution and that there are no extreme outliers. Similarly to the repeated measures ANOVA, the paired samples t-test is robust to violations of this assumption as long as the sample size is larger than 30 (Agresti & Franklin, 2009).

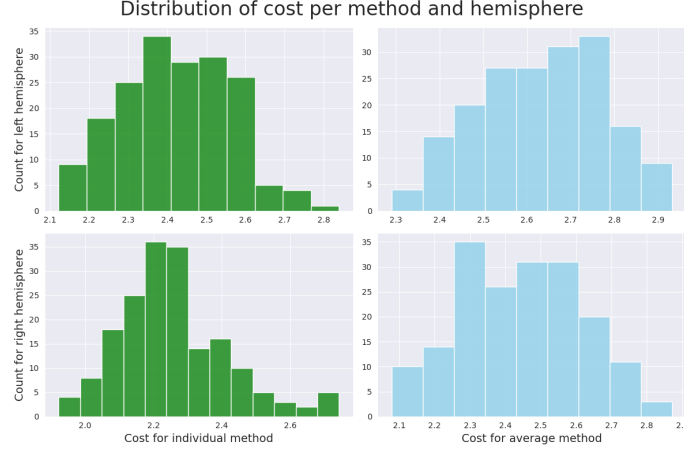


Figure 27. Histograms of the cost function for each method per hemisphere.

C Experiment 3 results

C.1 Descriptive results

Array type	Hem.	Max array	Dice loss	Yield loss	Prop. dice	HD	Prop. HD	Cost	Prop. cost
3d	LH	4.55	0.64	0.48	0.61	0.8	0.64	2.42	0.37
utah	LH	15.71	0.93	0.09	0.18	0.93	0.23	2.82	0.12
3d	RH	4.52	0.52	0.59	0.63	0.75	0.68	2.26	0.48
utah	RH	15.69	0.88	0.14	0.23	0.91	0.26	2.75	0.16

Table 11. Results table with average losses per array type and hemisphere for all 181 subjects.

Table 11 shows all mean metrics per hemisphere for each array type. As described for the results of experiment 1 in the appendix A.1, the proportional columns refer to the proportion that each metric covers relative to the scenario of stimulating all phosphene evoking neurons in V1.

C.2 Assumptions for paired samples t-test

The assumptions for the paired samples t-test are described in the appendix for experiment 2, B.2.

Figure 28 shows that the distributions of the cost function per hemisphere, for each array type, does not have any extreme outliers. Similarly to the repeated measures ANOVA, the paired samples t-test is robust to violations of the normality assumption as long as the sample size is larger than 30 (Agresti & Franklin, 2009), so all assumptions are met.

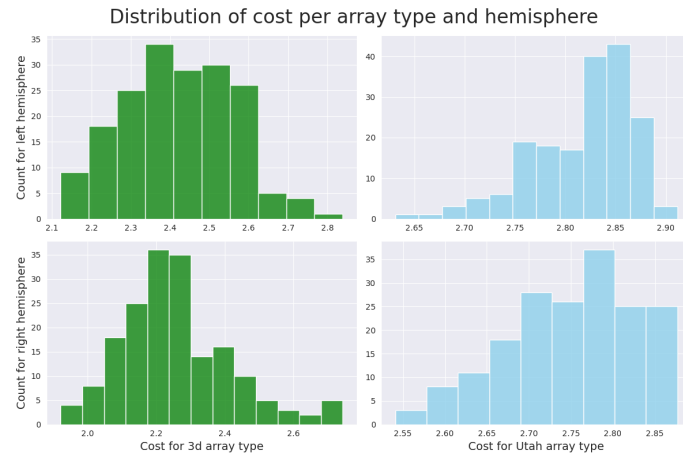


Figure 28. Histograms of the cost function for each array type per hemisphere.